Damping optimization of viscoelastic thin structures, application and analysis

Antoni Joubert, Grégoire Allaire, Samuel Amstutz, Julie Diani

Damping optimization of viscoelastic thin structures, application and analysis

Antoni Joubert[1*], Grégoire Allaire[2†], Samuel Amstutz[2†] and Julie Diani[1†]

[1]Laboratoire de Mécanique des Solides LMS, CNRS UMR 7649, École Polytechnique, Institut Polytechnique de Paris, Route de Saclay, 91128 Palaiseau, France.

[2]Centre de Mathématiques Appliquées CMAP, CNRS UMR 7641, École Polytechnique, Institut Polytechnique de Paris, Route de Saclay, 91128 Palaiseau, France.

*Corresponding author(s). E-mail(s): antoni.joubert1@outlook.fr;
Contributing authors: gregoire.allaire@polytechnique.fr;
samuel.amstutz@polytechnique.edu;
julie.diani@polytechnique.edu;
†These authors contributed equally to this work.

Abstract

In this work damping properties of bending viscoelastic thin structures are enhanced by topology optimization. Homogeneous linear viscoelastic plates are optimized and compared when modeled by either the Kirchhoff-Love or Reissner-Mindlin plate theories as well as by the bulk 3D viscoelastic constitutive equations. Mechanical equations are numerically solved by the finite element method and designs are represented by the level-set approach. High performance computing techniques allow to solve the transient viscoelastic problem for very thin 3D meshes, enabling a wider range of applications. The considered isotropic material is characterized by a generalized Maxwell model accounting for the viscoelasticity of both Young modulus and Poisson's ratio. Numerical results show considerable design differences according to the chosen mechanical model, and highlights a counter-intuitive section shrinking phenomenon discussed at length. The final numerical example extends the problem to an actual shoe sole application, performing its damping optimization in an industrial context.

Keywords: Free vibration, Damping, Linear viscoelasticity, Eigenvalue optimization, Optimal design

1 Introduction

Viscoelastic damping structures are widely used for vibration and noise reduction applications. They are commonly made of elastomers, or polymers within their glass transition, exhibiting both elastic and viscous characteristics when deforming. Thanks to the material viscosity, part of the mechanical energy is absorbed and dissipated as heat, providing good damping capabilities. The polymer viscoelastic properties, displaying several relaxation times well represented by rheological models such as the generalized Maxwell model, offer a large range of applications [1]. The current paper focuses on finding the optimal design of 2D and 3D thin structures at infinitesimal strain, in order to maximize their damping capacities. The problem is extended to an actual industrial application, the design of shoe soles [2]. For instance, high damping may be privileged for walking, while the contrary might be preferred for sport application where bouncing properties are favored [3]. Such an industrial application demands optimization within volume and compliance constraint. Moreover, the conception of such structures is typically performed in a decor-related manner, identifying the optimal design and material independently. In that respect, the current paper will focus on the necessary first milestone of defining the theoretical and numerical framework to calculate the optimal designs for a given linear viscoelastic polymer.

The optimal material distribution is reached using topology optimization methods. This shape optimization technique improves the distribution of material within a defined domain while supporting topological changes. These methods are extensively used within the elastic framework [4–6], and, in particular, topology optimization for transient response problems is a well-known topic [7–9]. The application of these techniques to the viscoelastic framework is a rather recent issue but has been tackled, nonetheless, through the use of various optimization techniques. Three main optimization categories have been employed, density-based, evolutionary and boundary variation methods. In the scope of transient response optimization of viscoelastic structures, density-based techniques are the most widely used. For instance, Andreassen and Jensen [10] maximized the attenuation of propagating waves by performing the topology optimization of periodic microstructures. The topology optimization of unconstrained layer damping (UCLD), conducted by Elsabbagh and Baz [11], aimed at optimizing the distribution of the viscoelastic treatment. More particularly, the popular solid isotropic material with penalization (SIMP) method has also been used in a several contributions. Kang et al. [12] optimized the distribution of damping material in damping layers for shell structures under harmonic excitations. Chen and Liu [13] employed the SIMP method to maximize the modal loss factor by carrying out the microstructural topology

optimization of viscoelastic structures. Fang et al. [14] performed the topology optimization of plates with constrained layer damping (CLD) treatments in order to maximize the modal loss factor. Furthermore, evolutionary methods have been applied in a viscoelastic framework, such as the Bidirectional Evolutionary Structural Optimization method [15] and the Evolutionary Structural Optimization (ESO) method [16]. Lastly, boundary variation methods applied in viscoelasticity are also present in the literature. Ansari et al. [17] followed a level-set approach to find the optimal distribution of CLD patches onto the surface of plate structures. Delgado and Hamdaoui [18] employed the level-set method to perform the structural optimization of multilayered and homogeneous viscoelastic structures. In a more recent paper [19], the authors went further on the optimization of homogeneous viscoelastic 2D plates using Hadamards boundary variation method. The damping of simple viscoelastic structures is maximized by simultaneously optimizing the thickness profile and the geometry, while considering the frequency dependence of Poisson's ratio.

The present contribution is in direct continuation, extending the shape optimization to topology optimization and advancing the mechanical model from the simple Kirchhoff-Love plate assumption to the Reissner-Mindlin theory and 3D general model. Level-set based topology optimizations have been performed in 2D and 3D. Model comparisons, performed in elasticity and viscoelasticty, show considerable design differences between 2D and 3D models with the creation of complex inner microstructures in 3D. Moreover, the results highlight a section shrinking phenomenon, also observed in other works [20–23], but exacerbated in the case of bending thin structures and leading to counter-intuitive designs. Therefore, a model analysis has been carried out, motivated by these surprising results, in order to compare the Kirchhoff-Love model, the Reissner-Mindlin theory and the general 3D model. While plate model comparison is a classical topic [24, 25], even in the scope of shape optimization [22, 26, 27], a better understanding of this critical shrinking phenomenon is proposed going progressively from 2D to 3D models.

This paper is organized as follows. Section 2 writes the problem setting for the damping optimization of thin structures. The viscoelastic plate models are presented and the optimization problem is detailed before providing the sensitivity analysis of the chosen objective function with respect to the design variables. Section 3 details the numerical implementation, the adaptation of the level-set method in a viscoelastic framework as well as the high performance computing techniques employed for the 3D simulations. The optimal designs have been estimated using finite elements methods. A model analysis is proposed in section 4, plate theories are first considered then compared to the general 3D linear viscoelastic model. Finally, an actual application to the damping of a shoe sole within industrial test constraints is provided in section 5 proving the robustness of the proposed algorithm.

2 Problem setting for damping topology optimization

The problem of interest is the free vibration of linear viscoelastic thin structures such as plates. Three models are studied and compared in this work, the Kirchhoff-Love and Reissner-Mindlin plate theories as well as a more general 3D model.

2.1 Viscoelastic plate models

The constitutive isotropic material is modeled by a classical generalized Maxwell model consisting in elementary Maxwell branches in parallel and an elastic branch for the long-term elasticity. The Young modulus, E, and Poisson's ratio, ν, are assumed to be associated to the same relaxation time, as represented in Figure 1 where n is the number of viscoelastic branches. Unlike in the current study, Poisson's ratio is often assumed constant, which is not strictly correct for polymers. Moreover, in the context of shape optimization, this assumption can lead to suboptimal results and inaccuracies for some materials [19].

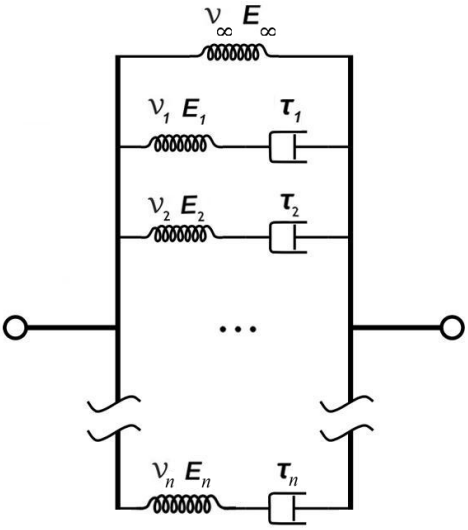

Fig. 1 Generalized Maxwell rheological scheme.

The working domain is the midsurface Ω of the 3D plate defined by

$$\Omega^{3D} = \left\{ (x_1, x_2, x_3) \in \mathbb{R}^3 \mid x_1 \in (0, L), x_2 \in \left(\frac{-W}{2}, \frac{W}{2} \right), x_3 \in \left(\frac{-h}{2}, \frac{h}{2} \right) \right\}. \tag{1}$$

The length of the plate is denoted L, the width W and the thickness h. Dirichlet conditions are applied on the clamped part Γ_D, at $x_1 = 0$, and stress-free

Neumann conditions are applied on the remaining boundaries Γ_N (Figure 2). In this paper, we focus on the out-of-plane displacement $U(x_1, x_2, t)$ and we

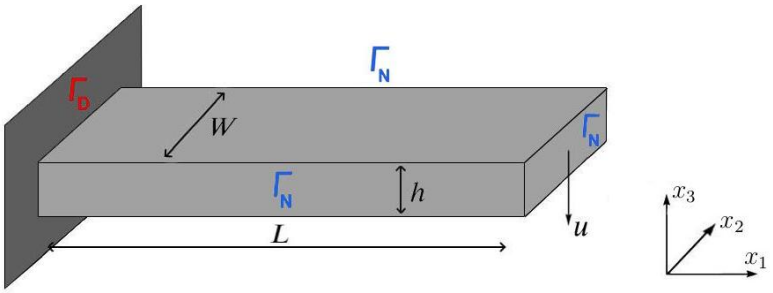

Fig. 2 Slender cantilever plate representation.

work in the frequency domain, assuming the displacement is harmonic such that

$$U(x_1, x_2, t) = u(x_1, x_2)e^{i\omega t}, \tag{2}$$

where ω is the pulsation of the system. Infinitesimal strain is also considered. The state equation in the case of the Kirchhoff-Love theory has been detailed in [19], leading to a complex polynomial eigenproblem.

In the following, we recall the procedure for the Reissner-Mindlin theory [28]. As opposed to the Kirchhoff-Love theory, the normals to the plate do not necessarily remain orthogonal to the mid-plane, accounting for transverse shear effects. This thick plate model assumes the displacement varies linearly and the transverse shear is constant across the plate thickness. For a displacement $\underline{U} = (U, \Theta_1, \Theta_2)$, where Θ_1 and Θ_2 denote respectively the rotations of the midsurface normal to the x_1 and x_2 axes, the linear plane strain tensor $\epsilon(U)$ is expressed as a 5-component vector

$$\epsilon = \begin{pmatrix} \epsilon_{11} \\ \epsilon_{22} \\ 2\epsilon_{12} \\ 2\epsilon_{13} \\ 2\epsilon_{23} \end{pmatrix} = \begin{pmatrix} -x_3 \dfrac{\partial \Theta_1}{\partial x_1} \\ -x_3 \dfrac{\partial \Theta_2}{\partial x_2} \\ -x_3 \left(\dfrac{\partial \Theta_1}{\partial x_2} + \dfrac{\partial \Theta_2}{\partial x_1} \right) \\ \dfrac{\partial U}{\partial x_1} - \Theta_1 \\ \dfrac{\partial U}{\partial x_2} - \Theta_2 \end{pmatrix}. \tag{3}$$

For the vibration problem, the displacement $\underline{U} = (U, \Theta_1, \Theta_2)$ is assumed harmonic, given by:

$$\begin{cases} U(x_1, x_2, t) = u(x_1, x_2)e^{i\omega t} \\ \Theta_1(x_1, x_2, t) = \theta_x(x_1, x_2)e^{i\omega t} \\ \Theta_2(x_1, x_2, t) = \theta_y(x_1, x_2)e^{i\omega t}. \end{cases} \tag{4}$$

As the shear stress profile in the thickness direction is known to be parabolic, assuming a constant shear strain is inaccurate. Consequently, a shear correction factor $\mathbf{k}$ is usually applied. The bending plane stress tensor is expressed as:

$$\sigma(x_1, x_2, x_3, t) = C_0\epsilon(\underline{U})(x_1, x_2, x_3, t) - \int_{-\infty}^{t} \frac{\partial R}{\partial \tau}(t-\tau)\epsilon(\underline{U})(x_1, x_2, x_3, \tau)d\tau, \tag{5}$$

where the first term represents the instantaneous response by

$$C_0\epsilon(\underline{U})(x_1, x_2, x_3, t) = \begin{bmatrix} c_{11} & c_{12} & 0 & 0 & 0 & \\ c_{12} & c_{22} & 0 & 0 & 0 & \\ 0 & 0 & c_{33} & 0 & 0 & 0 \\ 0 & 0 & 0 & \mathbf{k}\, c_{44} & 0 & \\ 0 & 0 & 0 & 0 & \mathbf{k}\, c_{55} & \end{bmatrix} \begin{pmatrix} \epsilon_{11} \\ \epsilon_{22} \\ 2\epsilon_{12} \\ 2\epsilon_{13} \\ 2\epsilon_{23} \end{pmatrix}$$

with

$$\begin{cases} c_{11} = c_{22} = \frac{E_\infty}{1-\nu_\infty^2} + \sum_{j=1}^{n} \frac{E_j}{1-\nu_j^2}, \\ c_{12} = \nu_\infty \frac{E_\infty}{1-\nu_\infty^2} + \sum_{j=1}^{n} \nu_j \frac{E_j}{1-\nu_j^2}, \\ c_{33} = c_{44} = c_{55} = \frac{E_\infty}{2(1+\nu_\infty)} + \sum_{j=1}^{n} \frac{E_j}{2(1+\nu_j)}. \end{cases}$$

The second term writes:

$$\int_{-\infty}^{t} \frac{\partial R}{\partial \tau}(t-\tau)\epsilon(\underline{U})(x_1, x_2, x_3, \tau)d\tau = \int_{-\infty}^{t} \begin{bmatrix} r_{11} & r_{12} & 0 & 0 & 0 \\ r_{12} & r_{22} & 0 & 0 & 0 \\ 0 & 0 & r_{33} & 0 & 0 \\ 0 & 0 & 0 & \mathbf{k}\, r_{44} & 0 \\ 0 & 0 & 0 & 0 & \mathbf{k}\, r_{55} \end{bmatrix} \begin{pmatrix} \epsilon_{11} \\ \epsilon_{22} \\ \gamma_{12} \\ \gamma_{13} \\ \gamma_{23} \end{pmatrix} d\tau$$

with

$$\begin{cases} r_{11} = r_{22} = \sum\limits_{j=1}^{n} \frac{E_j}{(1-\nu_j^2)\tau_j} e^{\frac{\tau-t}{\tau_j}}, \\ r_{12} = \sum\limits_{j=1}^{n} \frac{\nu_j E_j}{(1-\nu_j^2)\tau_j} e^{\frac{\tau-t}{\tau_j}}, \\ r_{33} = r_{44} = r_{55} = \sum\limits_{j=1}^{n} \frac{E_j}{2(1+\nu_j)\tau_j} e^{\frac{\tau-t}{\tau_j}}, \end{cases}$$

which becomes in the frequency domain

$$\int_{-\infty}^{t} \frac{\partial R}{\partial \tau}(t-\tau)\epsilon(\underline{U})(x_1,x_2,x_3,\tau)d\tau = \begin{bmatrix} \tilde{r}_{11} & \tilde{r}_{12} & 0 & 0 & 0 \\ \tilde{r}_{12} & \tilde{r}_{22} & 0 & 0 & 0 \\ 0 & 0 & \tilde{r}_{33} & 0 & 0 \\ 0 & 0 & 0 & \mathbf{k}\,\tilde{r}_{44} & 0 \\ 0 & 0 & 0 & 0 & \mathbf{k}\,\tilde{r}_{55} \end{bmatrix} \begin{pmatrix} -x_3 \dfrac{\partial \theta_1}{\partial x_1} \\ -x_3 \dfrac{\partial \theta_2}{\partial x_2} \\ -x_3 (\dfrac{\partial \theta_1}{\partial x_2} + \dfrac{\partial \theta_2}{\partial x_1}) \\ \dfrac{\partial u}{\partial x_1} - \theta_x \\ \dfrac{\partial u}{\partial x_2} - \theta_y \end{pmatrix} e^{i\omega t}$$

with

$$\begin{cases} \tilde{r}_{11} = \tilde{r}_{22} = \sum\limits_{j=1}^{n} \frac{E_j}{(1+i\omega\tau_j)(1-\nu_j^2)}, \\ \tilde{r}_{12} = \sum\limits_{j=1}^{n} \nu_j \frac{E_j}{(1+i\omega\tau_j)(1-\nu_j^2)}, \\ \tilde{r}_{33} = \tilde{r}_{44} = \tilde{r}_{55} = \sum\limits_{j=1}^{n} \frac{E_j}{2(1+i\omega\tau_j)(1+\nu_j)}. \end{cases}$$

The set of kinematically admissible displacements is defined by

$$\mathcal{U}_0 = \left\{ (u,\theta_1,\theta_2) \in \left(H^1(\Omega)\right)^3 \mid u_{\big|\Gamma_D} = 0, \theta_{1\big|\Gamma_D} = 0, \theta_{2\big|\Gamma_D} = 0 \right\}. \quad (6)$$

The principle of virtual power gives:
Find $\underline{U} = (U, \Theta_1, \Theta_2) \in \mathcal{U}_0$ such that

$$\int_{\Omega^{3D}} \rho \frac{\partial^2 U}{\partial t^2} \hat{U}\, dx + \int_{\Omega^{3D}} \rho x_3^2 \left(\frac{\partial^2 \Theta_1}{\partial t^2} \hat{\Theta}_1 + \frac{\partial^2 \Theta_2}{\partial t^2} \hat{\Theta}_2 \right) dx + \int_{\Omega^{3D}} \sigma \cdot \epsilon(\underline{\hat{U}})\, dx = 0 \quad \forall \underline{\hat{U}} \in \mathcal{U}_0. \quad (7)$$

The expressions of σ and $\epsilon(\hat{u})$ are then plugged in (7), and after explicit integration with respect to x_3, one obtains the spatial equation:

$$\forall \hat{\underline{u}} \in \mathcal{U}_0,$$

$$-\omega^2 \rho h \int_\Omega u\hat{u}\, dx - \omega^2 \rho \frac{h^3}{12} \int_\Omega \theta_x \hat{\theta}_x + \theta_y \hat{\theta}_y \, dx + \frac{h^3}{12} \int_\Omega \Bigg((c_{11} - \tilde{r}_{11}) \left(\frac{\partial \theta_x}{\partial x_1} \frac{\partial \hat{\theta}_x}{\partial x_1} + \frac{\partial \theta_y}{\partial x_2} \frac{\partial \hat{\theta}_y}{\partial x_2} \right)$$

$$+ (c_{12} - \tilde{r}_{12}) \left(\frac{\partial \theta_y}{\partial x_2} \frac{\partial \hat{\theta}_x}{\partial x_1} + \frac{\partial \theta_x}{\partial x_1} \frac{\partial \hat{\theta}_y}{\partial x_2} \right) + (c_{33} - \tilde{r}_{33}) \left(\frac{\partial \theta_x}{\partial x_2} + \frac{\partial \theta_y}{\partial x_1} \right) \left(\frac{\partial \hat{\theta}_x}{\partial x_2} + \frac{\partial \hat{\theta}_y}{\partial x_1} \right) \Bigg) dx$$

$$+ \mathbf{k} h \int_\Omega (c_{33} - \tilde{r}_{33}) \Bigg(\left(\frac{\partial u}{\partial x_1} - \theta_x \right) \left(\frac{\partial \hat{u}}{\partial x_1} - \hat{\theta}_x \right) + \left(\frac{\partial u}{\partial x_2} - \theta_y \right) \left(\frac{\partial \hat{u}}{\partial x_2} - \hat{\theta}_y \right) \Bigg) dx = 0. \tag{8}$$

Similarly to the the Kirchhoff-Love plate model, with $\underline{u} = (u, \theta_1, \theta_2)$, the equation can be rewritten as a complex polynomial eigenproblem in the form of

$$\sum_{j=0}^{n+2} \omega^j a_j(\underline{u}, \hat{\underline{u}}) = 0 \qquad \forall \hat{\underline{u}} \in \mathcal{U}_0. \tag{9}$$

The pulsation ω denotes the complex eigenvalue of the vibration problem, corresponding to the first mode of vibration, and a_j are complex symmetric bilinear forms independent of ω but dependent on the material parameters. This result naturally extends to 3D where the eigenproblem have the same form. Appendix A explicitly gives the expression of such bilinear forms for all three studied models. Eigenvalues are also assumed simple, otherwise the differentiability is lost. However, various methods to deal with multiple eigenvalues exist [29, 30].

2.2 Optimization problem

The first problem is the topology optimization of a vibrating viscoelastic structure, presented in Figure 3. The objective of the study is to maximize the vibration damping of a plate clamped at one edge, denoted Γ_{D1}, and stress-free at the remaining boundaries. In this example, the initial plate contains holes and the shape Ω is optimized in a domain denoted D.

Several objective functions allowing to characterize structural damping are reported in the literature, and compared in [19] within the framework of shape optimization. The modal loss factor [15, 31], logarithmic decrement [32] and decay rate [33, 34] are possible cost functions. The modal loss factor presents numerical instabilities in some cases and the decay rate is less interesting from an optimization point of view. Therefore, the selected quantity is the logarithmic decrement:

$$\mathcal{J}(\Omega) = -\frac{\mathrm{Im}(\omega)}{\mathrm{Re}(\omega)} \tag{10}$$

where the complex pulsation ω is obtained by solving the eigenproblem (9).

Furthermore, anticipating on later shoe sole optimization applications, a vertical load g is distributed along the width of the plate and a stiffness constraint is added. This constraint is based on the compliance, measured by the

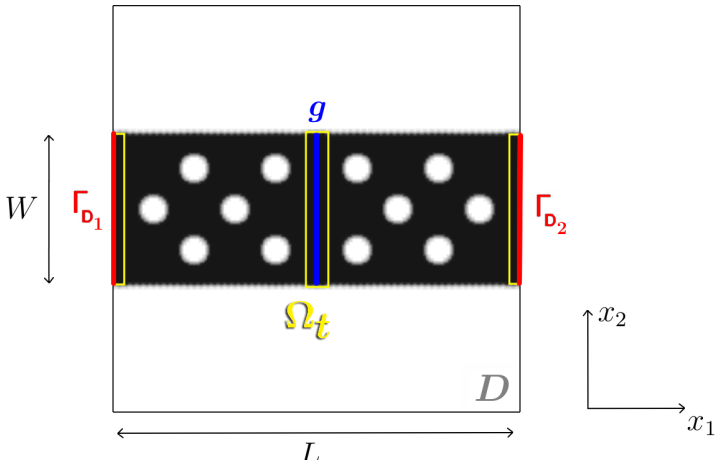

Fig. 3 Example of initialization of the plate topology optimization problem.

elastic strain energy as

$$C = \int_\Omega g u_g \, dx.$$

Note that the compliance is a global criterion, depending explicitly on the vertical displacement u_g, solution of a 3-point bending test, the plate being clamped at both ends. Since this problem is quasistatic, the displacement is determined by solving an elastic problem where the material parameters are chosen either instantaneous, $E_0 = E_\infty + \sum_{i=1}^{n} E_i$ and ν_0, or at equilibrium, E_∞ and ν_∞. In the following, rheological parameters at equilibrium were chosen. The equation of such problem for the Reissner-Mindlin theory is given by: Find $\underline{u}_g = (u_g, \theta_1, \theta_2) \in \mathcal{U}_1$ such that

$$\int_\Omega \frac{h^3}{12} D_b \kappa(\underline{u}_g) \cdot \kappa(\hat{\underline{u}}_g) \, dx + \int_\Omega h \mathbf{k} D_s \gamma(\underline{u}_g) \cdot \gamma(\hat{\underline{u}}_g) \, dx = \int_\Omega g \hat{u}_g \, dx \quad \forall \hat{\underline{u}}_g \in \mathcal{U}_1 \tag{11}$$

with

$$\mathcal{U}_1 = \left\{ (u_g, \theta_1, \theta_2) \in \left(H^1(\Omega)\right)^3 \mid u_g\big|_{\Gamma_{D_1}} = 0, \theta_1\big|_{\Gamma_{D_1}} = 0, \theta_2\big|_{\Gamma_{D_1}} = 0 \right\}, \tag{12}$$

where κ represents the bending strains and γ the shear strains, given by

$$\kappa = \begin{pmatrix} -\dfrac{\partial \theta_1}{\partial x_1} \\ -\dfrac{\partial \theta_2}{\partial x_2} \\ -\left(\dfrac{\partial \theta_1}{\partial x_2} + \dfrac{\partial \theta_2}{\partial x_1} \right) \end{pmatrix} \qquad \gamma = \begin{pmatrix} \dfrac{\partial u_g}{\partial x_1} - \theta_1 \\ \dfrac{\partial u_g}{\partial x_2} - \theta_2 \end{pmatrix}, \tag{13}$$

and where

$$D_b = \frac{E_\infty}{1-\nu_\infty^2}\begin{bmatrix} 1 & \nu_\infty & 0 \\ \nu_\infty & 1 & 0 \\ 0 & 0 & \frac{1-\nu_\infty}{2} \end{bmatrix} \qquad D_s = \frac{E_\infty}{2(1+\nu_\infty)}\begin{bmatrix} 1 & 0 \\ 0 & 1 \end{bmatrix}.$$

During the optimization, Γ_{D1} and Γ_{D2} are fixed and the remaining stress-free boundary Γ_N is subjected to optimization. Additionally, the material is fixed at the clamped boundaries and next to the application of the load, in a domain denoted Ω_t (Figure 3), to ensure boundary conditions are not altered during optimization. The constraint on the compliance, as well as the volume constraint, will be enforced by the augmented Lagrangian method. At each iteration, two problems are solved: a complex eigenproblem corresponding to the free-vibration of a viscoelastic plate, providing the eigenpair (ω, u) and the logarithmic decrement, and a quasistatic elastic problem, providing the vertical displacement u_g for a 3-point bending test and the compliance. The optimization problems finally writes:

$$\inf_{\Omega\in\mathcal{V}_{ad}} \mathcal{J}(\Omega) \text{ such that } C(\Omega) \leq C_l, \tag{14}$$

with

$$\mathcal{J}(\Omega) = -\frac{\mathrm{Im}(\omega(\Omega))}{\mathrm{Re}(\omega(\Omega))} \text{ and } C(\Omega) = \int_\Omega g u_g(x_1, x_2)\, dx, \tag{15}$$

where ω is the first pulsation, and C_l the compliance upper bound. The set of admissible shapes reads:

$$\mathcal{V}_{ad} = \{\Omega \in D \mid (\Gamma_{D_1} \cup \Gamma_{D_2}) \subset \partial\Omega, \Omega_t \subset \Omega\}.$$

2.3 Sensitivity analysis

Numerical resolution using a gradient method requires the computation of the shape derivative of the cost function. We work within the framework of Murat-Simon [35] following the spirit of Hadamard's method, see also [4, 36]. Given a reference domain Ω, we consider the perturbed domain

$$\Omega_\theta = (Id + \theta)\Omega \qquad \text{with} \qquad \theta \in W^{1,\infty}(\mathbb{R}^2, \mathbb{R}^2).$$

Where θ can be considered as a (bounded and Lipschitz) vector field advecting the reference domain. The map $(Id + \theta)$ is a bijection of $\mathbb{R}^2$ for any θ small enough in the norm of $W^{1,\infty}(\mathbb{R}^2, \mathbb{R}^2)$.

Definition 1 The shape derivative of a functional $F(\Omega_\theta)$ at Ω is the Fréchet derivative of the mapping $\theta \mapsto F((Id + \theta)\Omega)$ at $\theta = 0$ which can be expressed as follows:

$$F((Id+\theta)\Omega) = F(\Omega) + D_\Omega F(\Omega)\theta + o(\theta) \qquad \text{with} \qquad \lim_{\theta\to 0} \frac{|o(\theta)|}{\|\theta\|_{W^{1,\infty}}} = 0$$

for all $\theta \in W^{1,\infty}(\mathbb{R}^2, \mathbb{R}^2)$, where $D_\Omega F(\Omega)$ is a continuous linear form on $W^{1,\infty}(\mathbb{R}^2, \mathbb{R}^2)$ called the shape derivative of F.

We recall a classical result on the shape derivatives, see [4] for a proof.

Lemma 1 Given $f \in W^{1,1}(\mathbb{R}^2)$, consider the functional

$$F(\Omega) = \int_\Omega f(x)dx.$$

Then F is shape differentiable at Ω and its shape derivative is

$$D_\Omega F(\Omega)\theta = \int_\Omega \operatorname{div}\big(\theta(x)f(x)\big)dx = \int_{\partial\Omega} f(x)\theta(x).n(x)ds.$$

Of course, this result is also applicable to 3D domains. The transient problem, for which the dependence on the shape Ω has been highlighted, reads:

$$\sum_{j=0}^{n+2} \omega^j a_j(\Omega, u, \hat{u}) = 0 \qquad \forall \hat{u} \in \mathcal{U}_0, \tag{16}$$

where the complex symmetric bilinear forms are also written

$$a_j(\Omega, u, \hat{u}) = \int_\Omega g_j(u, \hat{u})dx \qquad \forall j \in [\![0, n+2]\!].$$

Proposition 1 *For any $\theta \in W^{1,\infty}(\mathbb{R}^2, \mathbb{R}^2)$ such that $\theta = 0$ on Γ_{D1}, $\Omega_t \subset \Omega$, and $(\omega, u) \in \mathbb{C} \times \mathcal{U}_0$ solution of (16), the shape derivative of $\mathcal{J}(\Omega)$ is given by*

$$D_\Omega \mathcal{J}(\Omega)\theta = -\int_{\Gamma_N} \frac{\operatorname{Re}(\omega)\operatorname{Im}\big(f(\omega,u)\big) - \operatorname{Im}(\omega)\operatorname{Re}\big(f(\omega,u)\big)}{\operatorname{Re}(\omega)^2}\, \theta \cdot n\, ds \tag{17}$$

where $f(\omega, u)$ is defined by

$$f(\omega, u) = -\frac{\sum_{j=0}^{n+2} \omega^j g_j(u, u)}{\sum_{j=1}^{n+2} j\omega^{j-1} a_j(\Omega, u, u)}. \tag{18}$$

See [19] for a proof. Note that, although the expression of a_j changes depending on the chosen model, they remain bilinear symmetric forms. Consequently, this proposition is applicable to either Kirchhoff-Love, Reissner-Mindlin or 3D models.

We also need to compute the shape derivative of the compliance, a classical result in topology optimization obtained using Lemma 1 and the self-adjoint

property of the problem. For $\underline{u}_g = (u_g, \theta_1, \theta_2)$ solution of (11), the shape derivative writes

$$D_\Omega C(\Omega)\theta = -\int_{\Gamma_N} \left(\frac{h^3}{12} D_b\kappa(\underline{u}_g) \cdot \kappa(\underline{u}_g) + h\mathbf{k} D_s\gamma(\underline{u}_g) \cdot \gamma(\underline{u}_g) \right) \theta \cdot n \, ds. \quad (19)$$

Following the same method, the shape derivative of the volume, given by $V(\Omega) = \int_\Omega h \, dx$, is expressed as

$$D_\Omega V(\Omega)\theta = \int_{\Gamma_N} h\theta \cdot n \, ds. \quad (20)$$

Note that there is no need to solve any adjoint problem because we work with functionals based on eigenvalues and the compliance.

3 Numerical implementation

Algorithms developed in this work are all implemented in FreeFem++ [37], an open-source PDE solver evaluating mechanical models by the finite element method. The optimization of Kirchhoff-Love plates, in particular, involves the resolution of a fourth-order problem set in a subspace of $H^2(\Omega)$, thus requiring conforming finite elements to be C^1. In this case, we chose non-conforming Morley elements, well-known to converge for fourth-order plate bending problems [38, 39]. Classical $\mathbb{P}_1$ triangular and $\mathbb{P}_1$ tetrahedral elements are used for the Reissner-Mindlin and 3D models respectively. Polynomial eigenproblems are solved using SLEPc solvers [40], interfaced with FreeFem++ [41, 42].

In order to minimize the objective function, we rely on a gradient descent algorithm and the level-set method. The numerical implementation, detailed for the 3D model, is easily adaptable to 2D plate models. Moreover, high performance computing techniques, for the 3D viscoelastic framework, are explained.

3.1 The level-set method in a viscoelastic framework

The level-set method, introduced by Osher and Sethian [43] and adapted to shape optimization in [44, 45], allows to numerically track the boundaries of the shape, representing $\Omega^{3D} \subset \mathbb{R}^3$ by a level-set function $\phi\colon D \mapsto \mathbb{R}$ defined as

$$\begin{cases} \phi(x) < 0 & \text{if } x \in \Omega^{3D} \\ \phi(x) = 0 & \text{if } x \in \partial\Omega^{3D} \\ \phi(x) > 0 & \text{if } x \in D \backslash \overline{\Omega^{3D}}, \end{cases} \quad (21)$$

where D is the working domain. The shape is deformed by advecting ϕ along a velocity field, usually oriented along the outward normal vector n, by solving

the advection equation

$$\frac{\partial \phi}{\partial t} + v(t,x)n(t,x).\nabla\phi = 0. \tag{22}$$

The normal velocity is denoted $v(t,x)$ and n is taken as

$$n(t,x) = \frac{\nabla\phi(x)}{|\nabla\phi(x)| + \eta_0},$$

where the small parameter η_0 has been added to avoid division by zero. The normal velocity is naturally chosen to be the integrand of the shape derivative of the cost function (17). In Freefem++, the advection of the level-set function is performed by the advect package, based on [46], solving the advection equation by the method of characteristics.

Additionally, a redistancing procedure of ϕ is implemented to ensure an accurate localization of $\partial\Omega^{3D}$, preventing large slopes close to the boundaries, and avoiding numerical instabilities due to small slopes. In FreeFem++, the redistancing of the level-set function is performed by a built-in fast marching algorithm. This procedure is applied every 10 iterations.

Constrained optimization problem

Geometric constraint are simply enforced by projection, using the expression:

$$P_{ad}(\phi) = \min\Big(\phi_c, \phi\Big), \tag{23}$$

where ϕ_c represents the non-optimizable domain, such as Ω_t in Figure 3, using simple algebraic functions. An augmented Lagrangian is employed to enforce the volume constraint as well as the compliance inequality constraint [47]. Although projection methods could be used for the volume constraint, the numerical cost is higher and the constraint is forced to be verified at each iteration, which, unlike the augmented Lagrangian method, may prevent early topological changes during the optimization.

The problem becomes:

$$\inf_{\Omega\in\mathcal{V}_{ad}} \sup_{\substack{\mu_1\geq 0\\ \mu_2\geq 0}} \mathcal{L}(\Omega,\mu), \tag{24}$$

with

$$\begin{aligned}\mathcal{L}(\Omega,\mu_1,\mu_2) = &-\frac{\mathrm{Im}(\omega(\Omega))}{\mathrm{Re}(\omega(\Omega))}\\ &+\frac{1}{2c_1}\Big(\big(P_{\mathcal{R}_+}(\mu_1 + c_1(C(\Omega)-C_l))\big)^2 - \mu_1^2\Big)\\ &+\mu_2(V(\Omega)-V_l) + \frac{c_2}{2}(V(\Omega)-V_l)^2\end{aligned} \tag{25}$$

where $\mu_1 \in \mathbb{R}$ and $c_1 \in \mathbb{R}_+$ are, respectively, the Lagrange multiplier and the penalization parameter for the compliance constraint, and $\mu_2 \in \mathbb{R}$ and $c_2 \in \mathbb{R}_+$ for the volume constraint. The target volume is also denoted V_l. In this work, a constant volume constraint is applied, therefore $V_l = V_0$ with V_0 the initial volume of the structure.

Extension and regularization procedure

The shape derivative of $\mathcal{L}(\Omega)$ is constructed from the linear combination of the shape derivative of the cost function (17), the compliance and the volume:

$$\begin{aligned} D_\Omega \mathcal{L}(\Omega)\theta = \int_{\partial\Omega_N} \Bigg(& - \frac{\mathrm{Re}(\omega)\,\mathrm{Im}\left(f(\omega,u)\right) - \mathrm{Im}(\omega)\,\mathrm{Re}\left(f(\omega,u)\right)}{\mathrm{Re}(\omega)^2} \\ & - P_{\mathcal{R}_+}\Big(\mu_1 + c_1\left(C(\Omega) - C_l\right)\Big)\Big(\sigma(u_g)\cdot\epsilon(u_g)\Big) \\ & + \Big(\mu_2 + c_2\left(V(\Omega) - V_l\right)\Big)\Bigg)\theta\cdot n\, ds, \end{aligned} \tag{26}$$

where

$$f(\omega,u) = -\frac{\sum_{j=0}^{n+2} \omega^j g_j(u,u)}{\sum_{j=1}^{n+2} j\omega^{j-1} a_j(\Omega,u,u)}.$$

To ensure smooth boundaries of the deformed shape, the shape derivative, initially defined on $\partial\Omega^{3D}$, is regularized and extended on the whole working domain D. This classical procedure is described in chapter 5 of [5]. More precisely, we rely on a regularization by the H^1 inner product:

$$\int_\Omega (\eta^2 \nabla\theta\cdot\nabla\hat{\theta} + \theta\cdot\hat{\theta})dx = -D_\Omega\mathcal{L}(\Omega)\hat{\theta} \qquad \forall\hat{\theta}\in H^1(\Omega), \tag{27}$$

which implies that the velocity field is solution of the system:

$$\begin{cases} -\eta^2\Delta\theta + \theta = 0 & \text{dans } D \\ \theta = 0 & \text{sur } \partial\Omega_{D_1}\cup\partial\Omega_{D_2} \\ \eta^2\dfrac{\partial\theta}{\partial n} = \Bigg(\dfrac{\mathrm{Re}(\omega)\,\mathrm{Im}\left(f(\omega,u)\right) - \mathrm{Im}(\omega)\,\mathrm{Re}\left(f(\omega,u)\right)}{\mathrm{Re}(\omega)^2} & \\ \quad + P_{\mathcal{R}_+}\Big(\mu_1 + c_1\left(C(\Omega) - C_l\right)\Big)\Big(\sigma(u_g)\cdot\epsilon(u_g)\Big) & \text{sur } \partial\Omega_N. \\ \quad - \Big(\mu_2 + c_2\left(V(\Omega) - V_l\right)\Big)\Bigg) n & \end{cases} \tag{28}$$

where η is the regularization parameter, usually of the order of a mesh size.

Ersatz material approximation

In the classical level-set method, mechanics equations are solved on a fixed mesh, in the entire working domain D. The void $D\backslash\Omega^{3D}$ is replaced by a weak "ersatz" material, usually characterized by a very small stiffness. In elasticity, one chooses typically $E^e \approx 10^{-5}E$ where E is the Young Modulus of the constitutive material. In the same vein, in linear viscoelasticity, E^e_∞ and $(E^e_j)_{j\in[\![1,n]\!]}$ are set to

$$E^e_j = E^e_\infty = 10^{-5}E_\infty \quad \forall j \in [\![1,n]\!]. \tag{29}$$

For simplicity purpose, Poisson's ratio and relaxation times are chosen to remain the same as the constitutive polymer. This work being focused on eigenvalues optimization, special care should be taken to ensure that the density is considerably smaller than the stiffness of the material [7], such that

$$\frac{\rho}{\rho^e} < \frac{E_j}{E^e_j} \quad \forall j \in [\![1,n]\!] \cup \{\infty\}. \tag{30}$$

This allows to avoid numerical instabilities and potential spurious modes since, in elasticity for instance, the smaller eigenvalues are of the order of the ratio $\frac{E}{\rho}$.

The ersatz approach presents clear advantages, for no remeshing is needed and all calculations can be performed on the same mesh. This does not come without drawbacks. First, the computational cost is higher as the state equations are solved on D, which is larger than Ω^{3D}. Second, it is necessary to define intermediate densities in the mesh elements containing $\partial\Omega^{3D}$. Various numerical solutions exist. One may consider using XFEM [48] or CutFEM [49] to cut, eliminate or enrich elements in order to precisely capture the boundaries of the shape. Another solution would be to remesh the whole domain D using a body-fitted mesh, with the MMG package [50] for instance. In the present study, we decide to define intermediate values for the viscoelastic modules, E^D_∞ and $(E^D_j)_{j\in[\![1,n]\!]}$, as $\mathbb{P}_0$ function defined on D by the expression:

$$E^D_j(\Omega) = f_v(\Omega)E_j + (1 - f_v(\Omega))\, E^e \quad \forall j \in [\![1,n]\!] \cup \{\infty\}, \tag{31}$$

where $f_v(\Omega)$ is the volume fraction of the mesh element that is inside the shape. Similarly, a density ρ^D is defined on D as a $\mathbb{P}_0$ function such that:

$$\rho^D(\Omega) = f_v(\Omega)\rho + (1 - f_v(\Omega))\rho^e, \tag{32}$$

where $\rho^e = 10^{-10}\rho$ denotes the ersatz density.

3.2 High performance computing

Mesh convergence studies performed on simple 3D bending elastic plates showed that a surprisingly large amount of elements in the structure thickness is required to achieve acceptable results. Consequently, the studied 3D shapes are represented by very thin meshes, making the use of parallel computing unavoidable. In this section, we detail the combined usage of FreeFem++,

OpenMPI, PETSc and SLEPc libraries applied to a damping optimization problem in linear viscoelasticity [42].

Each iteration of the optimization algorithm possesses the following structure:

1. Solve a complex polynomial eigenproblem in linear viscoelasticity
2. Solve a 3-point bending problem in linear elasticity
3. Update the optimization quantities (Lagrange multipliers, objective functions, ...)
4. Solve the shape gradient extension and regularization problem
5. Advection of the level-set function
6. Impose non-optimizable domain by projection
7. Apply a redistancing procedure (every 10 iterations)

Solving both state equations (step 1 and 2) is largely the most costly part of this algorithm. The advection of the level-set function and shape gradient extension problem are surprisingly inexpensive to compute. The algorithm is fully parallelized in FreeFEM++, except for the advection and redistancing procedure of the level-set (step 5 and 7) which are not yet compatible with parallel computing. The FreeFEM++ software comes with built-in OpenMPI and PETSc packages, allowing the concurrent use of FreeFEM++ and OpenMPI tools, as well as PETSc solvers and preconditioners. We compared various techniques and give, in the following, the most effective solver and preconditioner combinations for the present optimization problem.

A conjugate gradient solver and the GAMG preconditioner [51] are chosen to solve scalar problems, such as the extension of the shape gradient, with an algebraic multigrid method. The linear elastic bending problem is solved by the iterative solver GMRES [52] and the GAMG preconditioner, using an algebraic multigrid method with smoothing. Complex polynomial eigenproblems are solved with the TOAR (Two-level Orthogonal Arnoldi) solver from SLEPc, usable for an arbitrary polynomial degree, which build an Arnoldi factorization of the linearized problem. The associated linear problem is then solved by a direct solver from the library MUMPS (MUltifrontal Massively Parallel Solver) [53, 54], as using iterative solvers makes the procedure less robust. Using the symmetry of the eigenproblem, the Cholesky solver provides considerable computation time gains compared to the more general LU solver. Most iterative solvers require a domain decomposition, performed in FreeFem++ through the use of SCOTCH [55, 56] and METIS [57].

All numerical optimizations are performed on a cluster of 136 Intel Xeon Gold 6230 20-Core CPU, clocked at a frequency of 2.1 Ghz. The parallel computing of the complex polynomial eigenproblem is now of interest. Figure 4 represents the evolution of the speedup ratio and parallel efficiency, measures of scalability of the parallel system, with respect to the number of processors. For t_s the computational time in sequential and $t_p(n_p)$ the computational time

in parallel with n_p processors, the speedup ratio is defined by

$$A_c(n_p) = \frac{t_s}{t_p(n_p)},$$

and the parallel efficiency by

$$E_f(n_p) = \frac{A_c(n_p)}{n_p}.$$

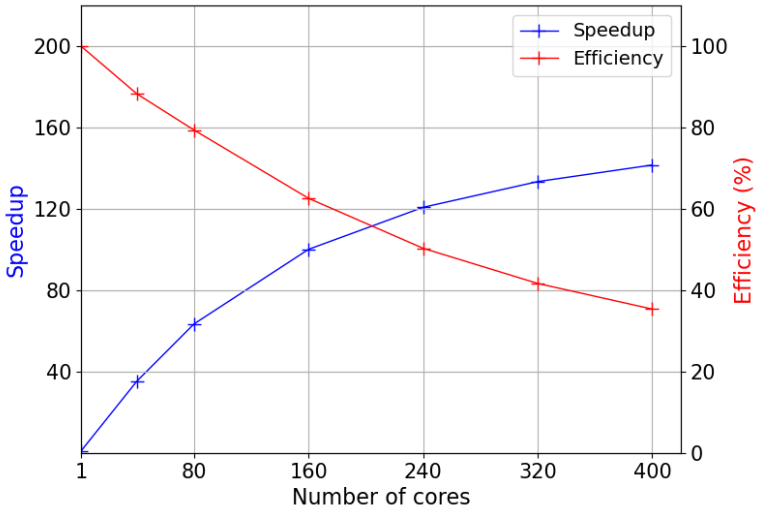

Fig. 4 Speedup ratio and parallel efficiency with respect to the number of cores, for a numerical test performed on the Cholesky cluster of Ecole Polytechnique on a mesh possessing 2 155 887 degrees of freedom.

As expected, the parallel efficiency decreases and the speedup ratio increases when the number of processor increases. It is important to note that no plateau has been reached, even with 400 processors, demonstrating good scaling in comparison to the elastic bending problem which requires less processors, usually between 40 and 80, before reaching a plateau. However, in term of computational cost, the resolution of the elastic problem is much faster than the viscoelastic eigenproblem. For the sake of computational efficiency, tests have been performed for a polymer modeled with a single relaxation time, meaning the degree of the polynomial is 3. The computational cost of the viscoelastic problem naturally increases with the degree. Increasing the accuracy of the rheological model means using larger relaxation time spectrums, resulting in polynomial eigenproblems of higher degrees, increasing drastically the computational duration. As a result, the usage of parallel computing is particularly relevant in such cases.

4 Model analysis

4.1 Optimal designs considering 2D models

This section is dedicated to the numerical results for the topology optimization of viscoelastic plates under free vibration. The objective is to maximize the structural damping of a structure with compliance and volume constraints. The plate of interest is represented in Figure 3, with an aspect ratio of $\frac{L}{W} = 2$, and is included in a 2D working domain D, discretized by a 100×100 structured mesh. The thickness is chosen constant $h = 3$ mm and the vertical load $g = 100$ N. All numerical results are obtained for a constant volume constraint $V_l = V_0$. For the sake of simplicity, in all viscoelastic examples, the constitutive polymer is characterized by a single relaxation time τ_1. Although theoretical and numerical results presented in this article are fully applicable to larger relaxation time spectrums. The material density is $\rho = 1000\ kg.m^{-3}$ and rheological parameters are $E_\infty = 18$ MPa, $E_1 = 30$ MPa, $\tau_1 = 0.002$ s, $\nu_\infty = 0.499$, $\nu_1 = 0.498$. Note that the relaxation time value has been chosen to scale well with the structure free vibration period.

Damping optimization of viscoelastic plates

A Kirchhoff-Love plate is first considered. The objective is to maximize the structural damping while keeping the same volume and increasing the bending stiffness by 15% ($C_l = 0.85C_0$). The optimization results of problem (24) are given in Figure 5a, showing the evolution of the design, and Figure 5b, comparing the vibration behavior of the initial and optimized plates. We also

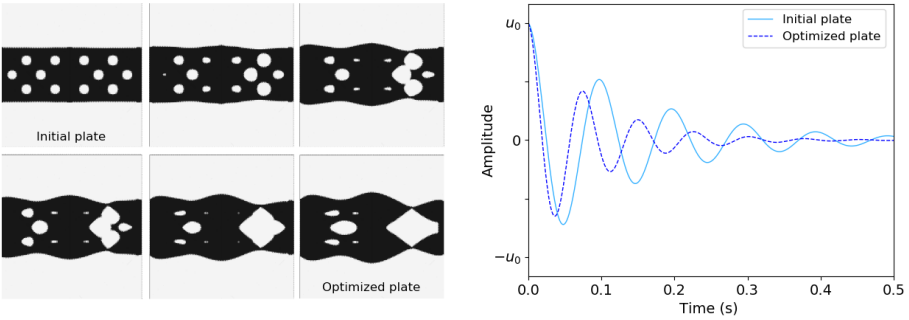

(a) (b)

Fig. 5 (a) Design evolution of the viscoelastic plate during the optimization process and (b) free vibration amplitudes of the initial and optimized structures for a generalized Maxwell material.

verify the convergence of the Lagrangian, and so the algorithm, in Figure 6a. In Figure 5a, one notices a material accumulation at the clamped boundary of the free vibration test, Γ_{D1}, but also a structural reinforcement close to the application of the load, at the center of the plate. Concerning weak sections

appear between the load and the right clamped boundary Γ_{D2}. This design is counter-intuitive as the compliance has been decrease by 15%, as shown by the compliance convergence plotted in Figure 6b. The optimal design, although seemingly weak, displays much better damping performances than the initial design for a relative gain of 35%.

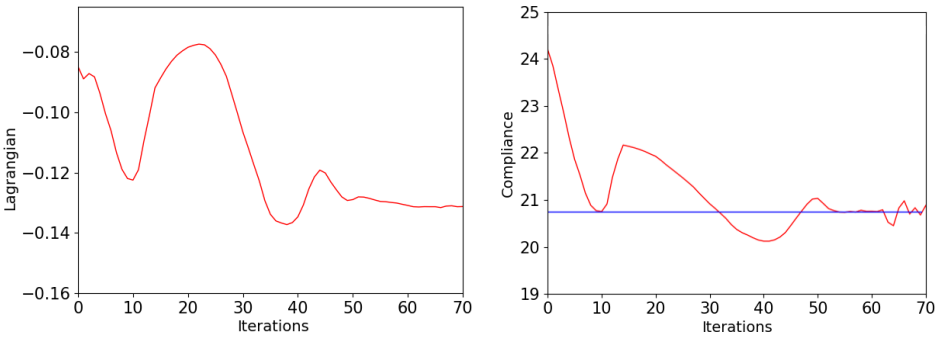

Fig. 6 (a) Convergence curve of the Lagrangian of the damping optimization problem of a 2D viscoelastic plate and (b) the evolution of the compliance during the optimization process.

Other examples were studied for various compliance constraints. While considerably different, numerical results showed the same tendencies. The design is reinforced at the clamped boundaries and near the application of the load but also presents weak spots at the same location.

Topology optimization results are usually highly dependent on the initialization. In this problem in particular, only the number of "weak branches" changes. The number of weak spots increases with the initial number of holes but does not seem to alter the damping performances of the structure.

In order to better understand the section shrinking phenomenon highlighted by the previous example, several numerical tests are performed in linear elasticity, with various plate models and optimization parameters.

Stiffness optimization of elastic bending plates

Classical compliance minimization problems are now studied for elastic bending plates. The material parameters are chosen arbitrarily as $E = 18$ MPa and $\nu = 0.499$, which could represent a polymer network well above its glass transition. Figure 7a illustrates the initial plate, simply clamped at one edge Γ_{D1} and submitted to a vertical load g at the free opposite end. The same geometric constraint, denoted Ω_e, is enforced, fixing the material close to the boundary conditions, represented in yellow in Figure 7a. Optimization design for the Kirchhoff-Love model is shown Figure 7b, where the shrinking phenomenon can still be noticed, at the free end of the plate, thus discarding the effects of the viscoelastic model.

A potential source of error is the approximation made by using a thin plate theory. The problem is now solved with Reissner-Mindlin assumptions. We recall that this thick plate model assumes the displacement varies linearly and the transverse shear is constant across the plate thickness. The final design, shown in Figure 7c, is very close to the result obtained for the Kirchhoff-Love model, displaying the same shrinking phenomenon. Therefore, neglecting the transverse shear effects is not responsible for the appearance of counter-intuitive weak sections.

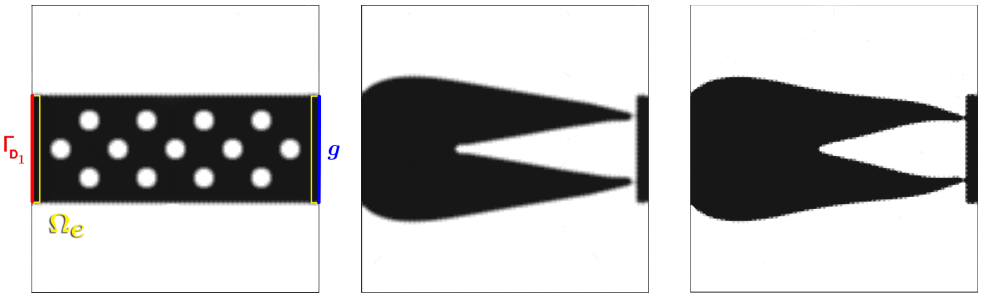

Fig. 7 (a) Initial design and optimal designs for the bending compliance minimization of (b) a Kirchhoff-Love plate and (c) a Reissner-Mindlin elastic plate.

Thin areas present transverse shear concentrations but, in view of the section thinness, one could expect much higher stress concentration. Another possible explanation would be the chosen cost function, or, in the viscoelastic case, the chosen constraint. The compliance is a global quantity, explicitly dependent on the displacement. As weak spots, acting as pivots, are close to the application of the load, only a slight increase in displacement is observed, leading to a small increase in compliance. However, increasing the width of the fixed band of material at the free end of plate has no effect on the phenomenon, although weak spots now remain further from the application of the load.

Several other possibilities have to be mentioned:

- Plate theories may be insufficient to accurately represent the bending stiffness of a thin structure. This does not seem to be limited to the Kirchhoff-Love model as the richer Reissner-Mindlin model also presents the same section shrinking phenomenon.
- As expected, the first derivative of the rotation $\dfrac{\partial \theta_1}{\partial x_1}$ drastically increases near the singularities. In fact, if we consider the thin branches as cantilevers, we know that $\dfrac{\partial \theta_1}{\partial x_1} \propto \dfrac{1}{I}$, with I the quadratic moment of area. For the Kirchhoff-Love model for instance, as $\theta_1 \approx \dfrac{\partial u}{\partial x_1}$, the displacement field u is a lot smoother than $\dfrac{\partial \theta_1}{\partial x_1}$. The compliance being explicitly dependent on the

displacement, the impact of the weak spots on the final performances may have been smoothed.
- Finally, we recall that the compliance is a global criterion. Consequently, it is possible to see locally low stiffness areas, as long as the global stiffness of the structure is not undermined.

More general but similar optimization problems are frequently investigated in the literature, notably in 2D, with different boundary conditions [20–23]. Although less pronounced, the same section shrinking phenomenon can be observed.

Hence, the singularities either come from plate models or cost function limitations. This naturally leads to the extension to 3D optimization algorithms in order to better understand the phenomenon.

4.2 Extension to 3D

Two problems are of interest, the compliance minimization of an elastic plate and the damping maximization of a viscoelastic plate under free vibration, both 3D equivalent of the 2D optimization problems studied in the previous section. The 3D viscoelastic damping optimization is an important step toward potential 3D applications, whereas the classical 3D elastic optimization mainly aims at completing the study of the section shrinking phenomenon. The elastic and viscoelastic materials involved remain the same. The aspect ratio of the plate is also unchanged, but the working domain is now discretized by a 3D structured mesh using $\mathbb{P}_1$ tetrahedral elements.

Stiffness optimization of a bending elastic plate in 3D

In this example, the mesh is particularly fine, with a size of $250 \times 250 \times 25$, corresponding to 4 914 078 degrees of freedom. The initial design, described by the initial level-set function, is given as a half-cut in Figure 8. Various final designs, but displaying analogous performances, were obtained for different initializations. As observations are also similar, we decide to show the numerical results for an initial structure chosen arbitrarily. Boundary conditions as well as geometric constraints are simply the 3D equivalent of the previous 2D elastic plate optimization. The topology optimization is carried out on 80 cores, with a domain decomposed in 80 sub-domains. In this case, the computational time is 8 hours. Figure 9 shows the evolution of the compliance and volume throughout the optimization. The minimization of the objective function as well as the enforcement of the volume constraint can then be verified. The final design, represented in Figure 10, shows reinforcement at the clamped boundary. Weak spots are still present, although more robust than 2D optimized plates due to a complex inner pattern, as revealed by Figure 11, which are multiple cantilevers oriented in the thickness of the plate, increasing the bending stiffness of the structure.

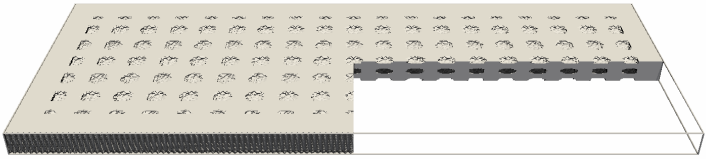

Fig. 8 Initialization of the topology optimization of a 3D bending elastic plate using the level-set method.

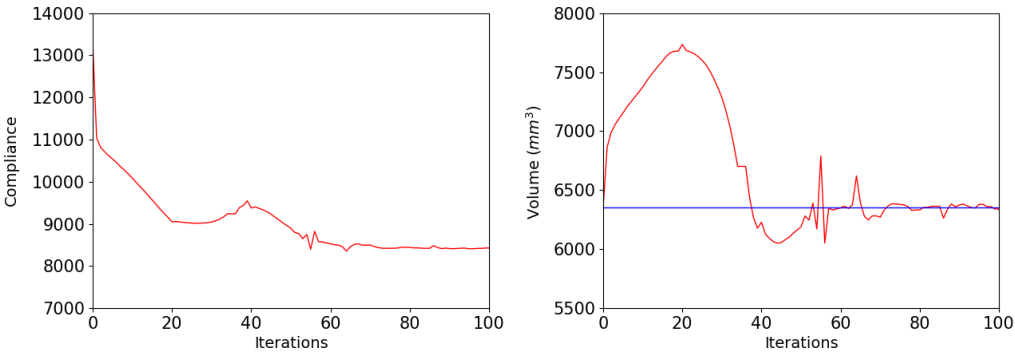

(a) (b)

Fig. 9 Evolution of (a) the compliance and (b) volume during the compliance minimization of an elastic 3D bending plate.

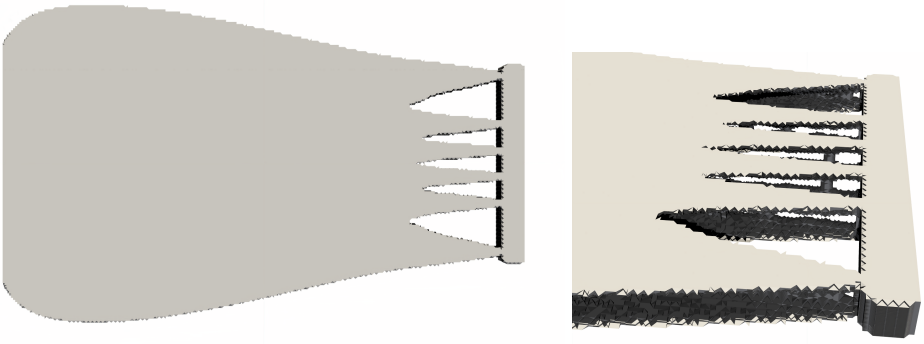

(a) (b)

Fig. 10 (a) Final design of the 3D elastic bending plate and (b) zoom in of the connection between the plate and the non-optimizable domain.

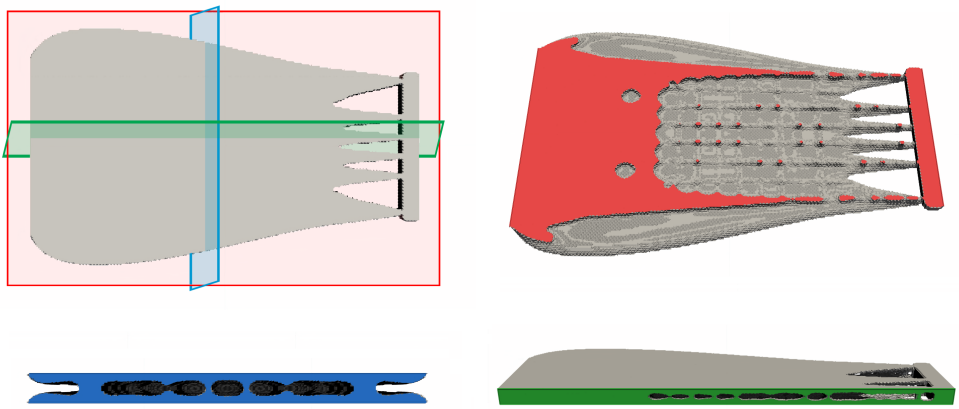

Fig. 11 Cuts of the optimized 3D elastic plate for various cutting planes.

The obtained 3D optimal design possesses an interesting and complex topology, not accessible with 2D models. The appearance of short vertical cantilevers is a remarkable result, considering the compliance is a classical objective function. Therefore, 3D optimization techniques seem required for compliance minimization problems of bending thin structures.

Damping optimization of a 3D viscoelastic plate

As solving complex polynomial eigenproblems is costly, the chosen mesh is coarser than the previous example, with a size of $200 \times 200 \times 20$, corresponding to 2 545 263 degrees of freedom. The same initial design is used to perform the topology optimization of a 3D viscoelastic plate. The objective is to maximize the structural damping while keeping the same volume and enforcing a compliance constraint. In this example, the constraint is $C_l = 0.85C_0$, similar to the 2D viscoelastic case. The optimization is performed on 400 cores, with a mesh decomposed in 400 sub-domains. The computations now last approximately 12 hours, and most of this duration is dedicated to the resolution of viscoelastic eigenproblems. The final design, represented in Figure 12a, shows reinforcements at the clamped boundary $\partial\Omega_{D1}$ and near the application of the load. Weak spots are also present, due to the compliance constraint, but are more robust. The optimized design shows the same tendencies as its 2D equivalent, except an inner structure is now present, illustrated in Figure 13, increasing the bending stiffness and allowing to enforce the compliance constraint. The vibration behavior of the optimized plate is compared to the initialization in Figure 12b. The use of 3D optimization techniques enables to reach better performing structures as the relative structural damping gain is 73%, considerably higher than the 35% gain obtained in 2D.

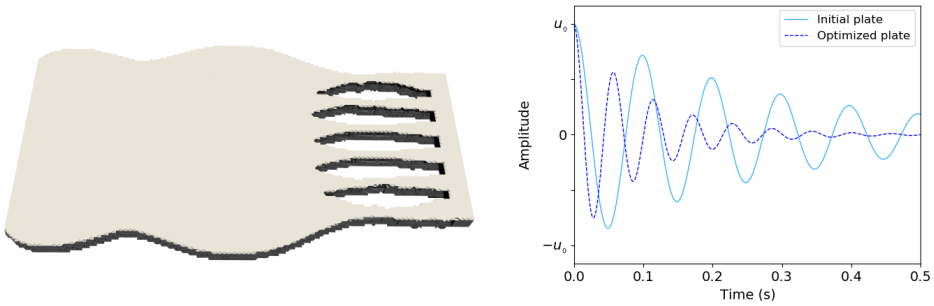

(a) (b)

Fig. 12 (a) Optimized plate and (b) vibration behavior comparison of the initial and final designs for the damping maximization of a 3D viscoelastic plate.

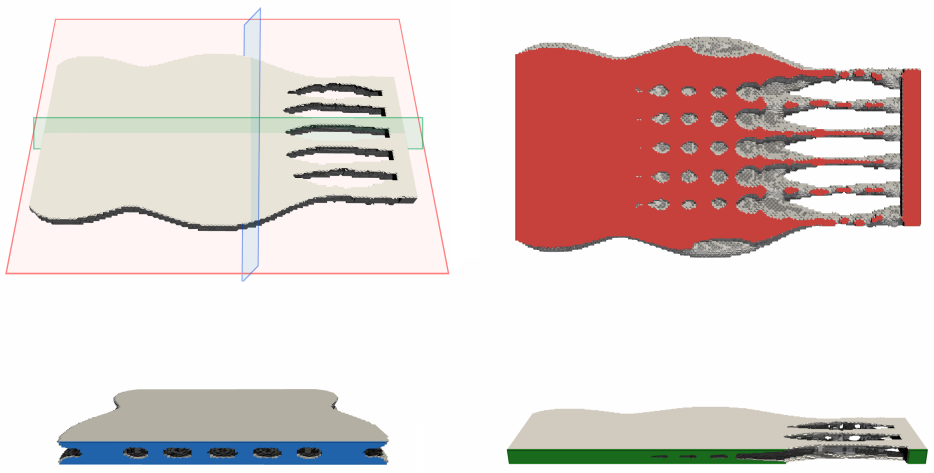

Fig. 13 Cuts of the optimal design of a viscoelastic plate under free vibration for several perpendicular planes.

The optimal design shows important damping gains, partly due to inner topological details only obtainable through 3D modelization. From an application point of view, the structure remains unsatisfactory as the design is locally weak where sections are thin. Several numerical techniques exist to prevent such phenomenon. One simple solution, for instance, is to use a minimum thickness constraint [58, 59]. However, in this article, the application of interest is the running shoe sole, and, as detailed in the next section, changing the optimization problem according to industrial needs has been enough to avoid the apparition of weak spots.

5 Extension to actual shoe sole application

We now consider a less academic application of topology optimization to the design of a shoe sole. It is important to note that this example is focused on an optimization with respect to classical industrial tests, not in real conditions of use. Three mechanical tests are usually performed:

- Free vibration tests, where the shoe sole is clamped at one end and submitted to an initial displacement at the opposite end. Either high damping or high bouncing properties are desired. In this article, we focus on the damping maximization.
- A 3-point bending test, such as the Bennewart test, reproduces a typical load applied on the sole by a customer, also commonly used as a fatigue test. This criterion is taken into account as a compliance constraint.
- A torsion test, for specific sport applications, can also be considered. Although easily addressable by adding an optimization constraint, like the compliance constraint, this mechanical test will be set aside for the sake of simplicity.

5.1 Damping optimization problem

Optimized plates obtained in the previous section are reinforced near the clamped boundary related to the free vibration problem, $\partial\Omega_{D1}$. This inevitably weakens the opposite end of the structure, thus drastically decreasing the structural damping for a plate clamped at $\partial\Omega_{D2}$. From an industrial point of view, the structure is expected to possess good performances regardless of the chosen clamped boundary. Therefore, a second vibration problem is considered. The objective function becomes the sum of two logarithmic decrements:

$$\mathcal{J}(\Omega) = -\frac{\mathrm{Im}(\omega^{D1})(\Omega)}{\mathrm{Re}(\omega^{D1})(\Omega)} - \frac{\mathrm{Im}(\omega^{D2})(\Omega)}{\mathrm{Re}(\omega^{D2})(\Omega)} \tag{33}$$

where ω^{D1} and ω^{D2} are the pulsations corresponding to the vibration tests for a structure clamped at $\partial\Omega_{D1}$ and $\partial\Omega_{D2}$ respectively. For the sake of readability, the 3D shape Ω^{3D} is simply denoted Ω. The volume and compliance constraints are still enforced by an augmented Lagrangian method. The problem now reads:

$$\inf_{\Omega\in\mathcal{W}_{ad}} \sup_{\substack{\mu_1\geq 0\\ \mu_2\geq 0}} \mathcal{L}(\Omega,\mu), \tag{34}$$

where

$$\begin{aligned}\mathcal{L}(\Omega,\mu_1,\mu_2) = &-\frac{\mathrm{Im}(\omega^{D1})(\Omega)}{\mathrm{Re}(\omega^{D1})(\Omega)} - \frac{\mathrm{Im}(\omega^{D2})(\Omega)}{\mathrm{Re}(\omega^{D2})(\Omega)}\\ &+\frac{1}{2c_1}\left(\left(P_{\mathcal{R}_+}(\mu_1+c_1(C(\Omega)-C_l))\right)^2-\mu_1^2\right)\\ &+\mu_2(V(\Omega)-V_l)+\frac{c_2}{2}(V(\Omega)-V_l)^2\end{aligned} \tag{35}$$

and

$$\mathcal{W}_{ad} = \{\Omega \in D \mid (\partial\Omega_{D_1} \cup \partial\Omega_{D_2}) \subset \partial\Omega, \Omega_t \subset \Omega\}.$$

Initial conditions are shown in Figure 14a, for a 3D plate, and adapted to the running shoe sole in Figure 14b. Note that, in the latter case, the working domain D has a sole-like design, fixing the global shape of the structure.

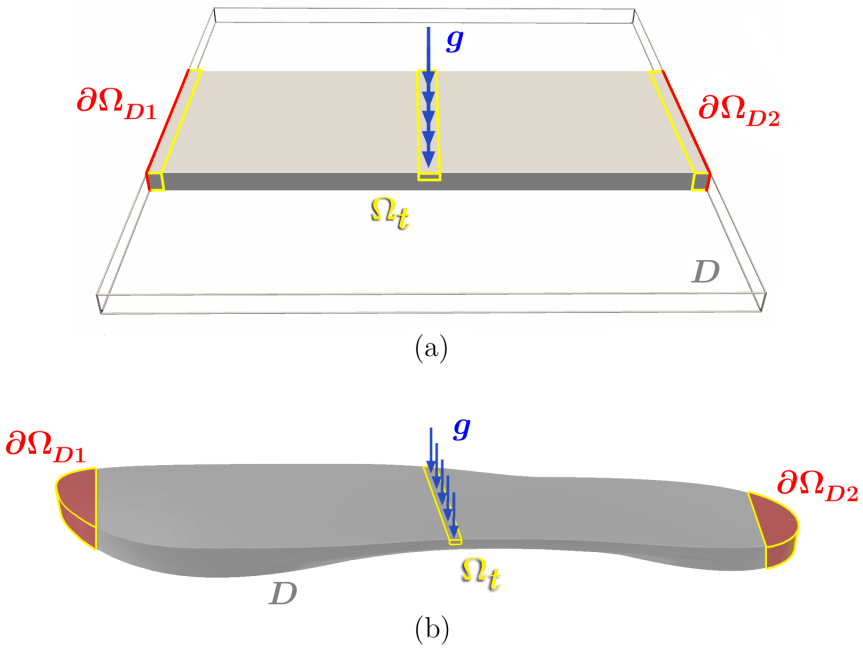

Fig. 14 Boundary conditions and geometric constraints of (a) the 3D viscoelastic plate and (b) the viscoelastic shoe sole optimization problems.

5.2 Numerical examples

The introduction of a second vibration test induces a second viscoelastic eigenproblem. For each optimization iteration, one must solve two complex polynomial eigenproblems and an elastic 3-point bending problem. The computational cost of the optimization considerably increases as a result. Two examples are presented in this section. The enriched objective function is first minimized for a simple 3D viscoelastic plate, then the optimization problem is solved for a typical shoe sole.

3D viscoelastic plate optimization

The topology optimization of a 3D plate is performed in a working domain discretized by the same $200 \times 200 \times 20$ structured mesh. The introduction of a second eigenproblem brings the computational cost to 20 hours, for 400 cores

and sub-domains. In this example, the compliance constraint is chosen as $C_l = 0.7C_0$. Keeping the same level-set initialization (Figure 8), the optimal design is given in Figure 15. Various cuts are also provided in Figure 16. Similarly to

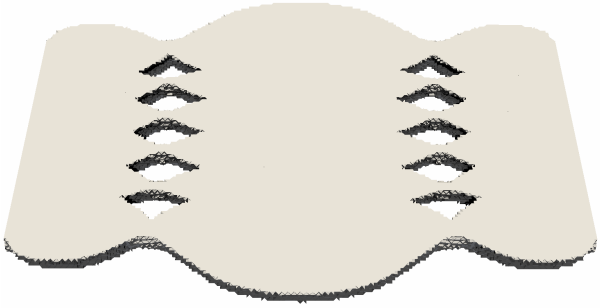

Fig. 15 Final design of the damping maximization problem of a viscoelastic plate under free vibration for two clamped boundary configurations.

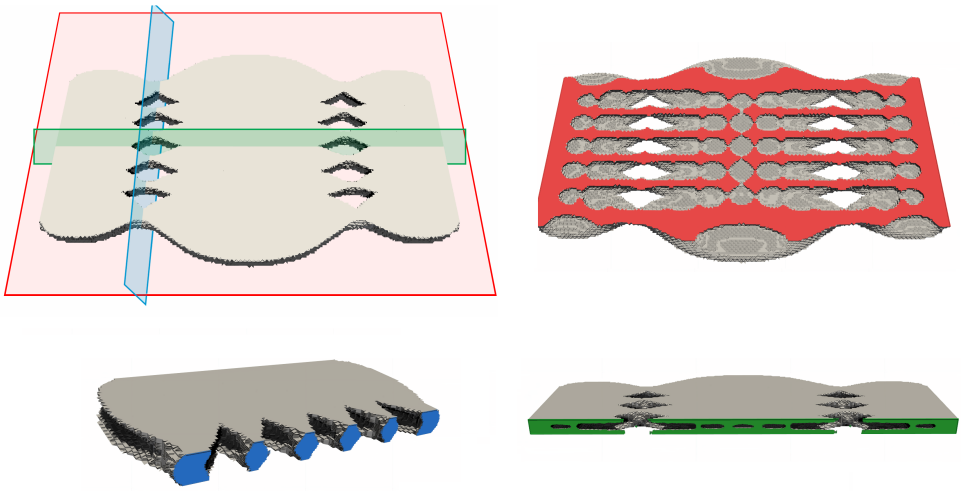

Fig. 16 Inside design of the optimized 3D viscoelastic plate for different cutting planes.

the results obtained in the previous section, thinner sections appear, although much more robust, as highlighted by the blue cut, due to the proximity to a clamped boundary. A complex inner microstructure can also be noticed, as shown by the red cut, allowing to satisfy the compliance constraint. Figure 17 compares the vibration behavior of the final and initial design, for both

vibration problem. Since the structure has several planes of symmetry, relative gains are similar in both cases, approximately 6.2%, for a total of 12.4%, which is much lower than previous examples. This is due to the fact that both vibration problems are acting in opposition. The optimal design is simply a trade-off, ensuring damping gains for both clamped configurations. Besides, the chosen compliance constraint is rather strong in this example, reducing the gains even more. We verify in Figure 18 that the compliance and volume constraints have been enforced.

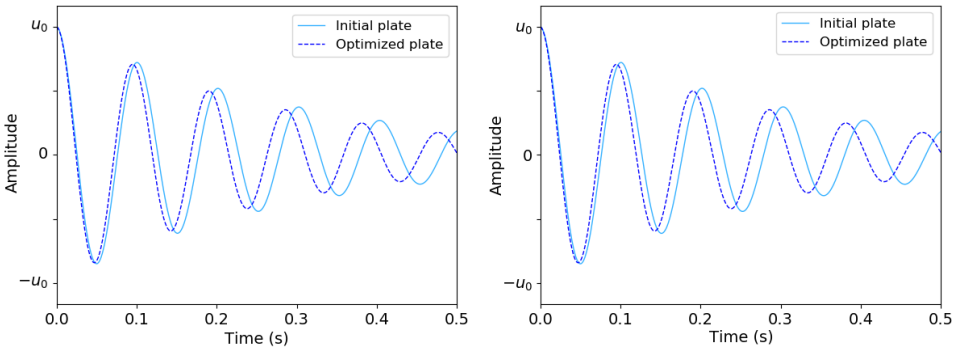

Fig. 17 Vibration behavior comparison of the initial and optimal designs for (a) $\partial\Omega_{D1}$ and (b) $\partial\Omega_{D2}$ as clamped boundary.

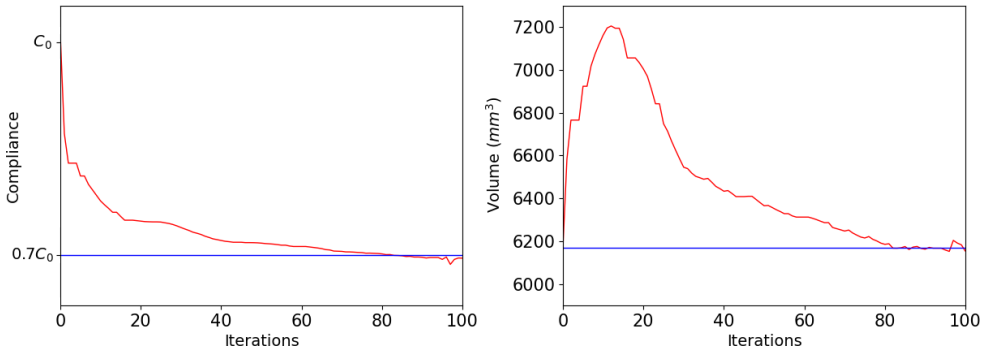

Fig. 18 Evolution of (a) the compliance and (b) volume during the topology optimization of a viscoelastic plate under free vibration.

Taking into account two vibration problems allows to obtain more balanced designs, satisfying industrial needs while avoiding the apparition of very thin sections, which are not acceptable for future applications. This new enriched optimization problem also comes with a performance decrease, as expected when optimizing a structure with respect to two opposite vibration problems.

Optimization of a running shoe sole

The same topology optimization is performed on a new unstructured mesh, created with the software Gmsh [60], from a CAD made on CATIA V5 [61]. The mesh has 1 334 484 degrees of freedom and the computational duration is 15 hours, for 400 cores and sub-domains. The compliance constraint is chosen as $C_l = 0.75C_0$. A new level-set initialization is used, representing the initial design shown in Figure 19.

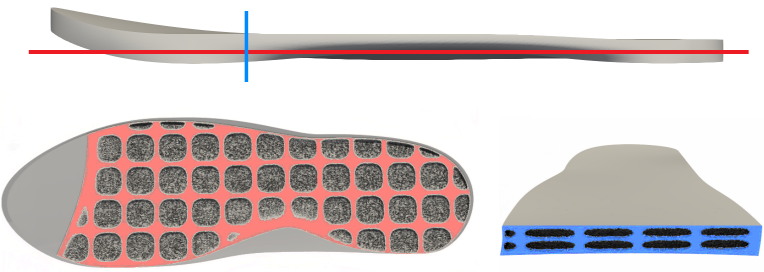

Fig. 19 Shoe sole design corresponding to the initial level-set function.

Different views and cuts of the optimal design are presented in Figure 20 and 21. The optimized shoe sole displays the same tendencies, the structure is reinforced at the free ends, at the middle and shows a complex inner structure, see the red cut. Similarly to the previous example, the thinner sections are robust, as highlighted by the blue cut.

Unlike plate topology optimizations, neither the initial nor final designs present any planes of symmetry. As a result, structural damping gains are not the same for both vibration problems, 8% and 9% for a structure clamped at $\partial\Omega_{D1}$ and $\partial\Omega_{D2}$ respectively, for a total relative gain of 17%, see Figure 22. The optimal design shows better damping performances and, as illustrated Figure 23, an increased bending stiffness, while maintaining the same volume.

Finally, let us mention that the optimized shoe sole, although better performing according to industrial criterions, presents holes in areas where the user applies the maximum vertical load. Therefore, the results also highlight that typical industrial tests are insufficient to adequately perform the damping optimization of a shoe sole under normal operating conditions.

Fig. 20 Various views of the optimized sports shoe sole for the damping maximization of the structure.

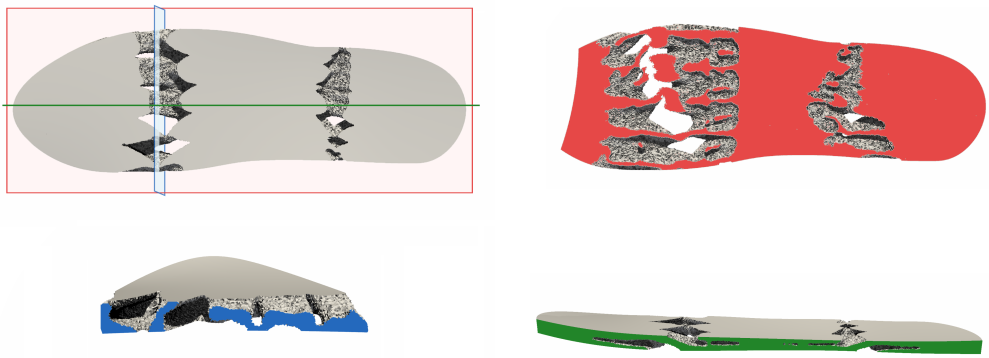

Fig. 21 Inside final design of the optimized viscoelastic shoe sole for different cutting planes.

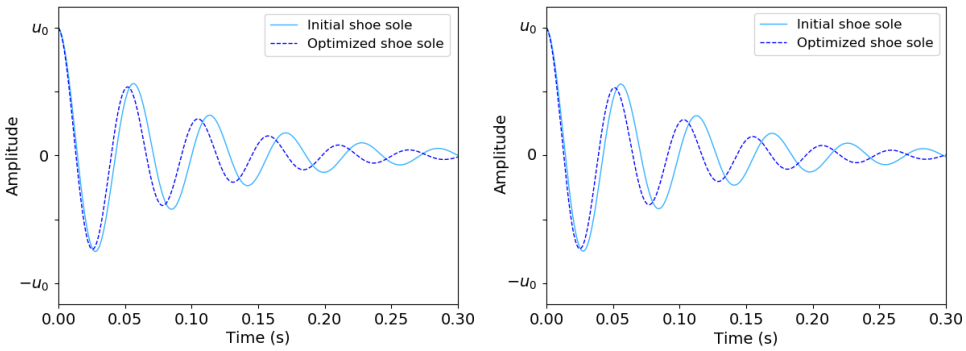

Fig. 22 Free vibration behavior comparison between the initial and optimized shoe soles with (a) $\partial\Omega_{D1}$ and (b) $\partial\Omega_{D2}$ as clamped boundary.

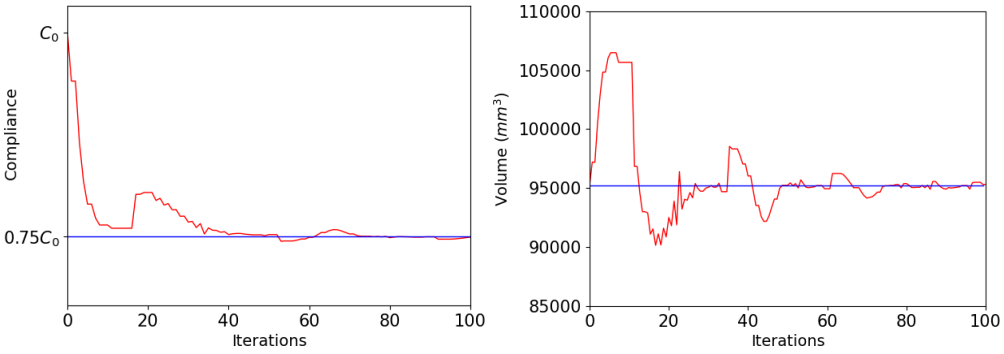

Fig. 23 (a) Compliance and (b) volume evolution during the topology optimization of a viscoelastic shoe sole.

6 Conclusion

The theoretical topology optimization problem has been written for the case of viscoelastic thin structures under free vibration within volume and compliance constraints. The material is represented by a linear generalized Maxwell model accounting for both Young modulus and Poisson's ratio viscoelasticity. The constitutive equations are written either with the Kirchhoff-Love model, the Reissner-Mindlin theory or the general 3D linear viscoelasticity framework. The optimization algorithms have been developed using a level-set approach within a classic finite element analysis. Simple 2D representations have been chosen for the plate models while high performance computing techniques have been required for running 3D vibration simulations.

Albeit the structural damping has been successfully enhanced, the final optimization designs have shown consistently section shrinking phenomena for every model due to the chosen global criterion of compliance optimization. However, it was observed that 3D modeling, as opposed to the plate models, creates inner microstructure designs such as cantilevers, making the design more mechanically acceptable.

Finally, the 3D damping optimization problem has been extended to a shoe sole design within industrial test constraints. Results proved the algorithm robustness but also revealed the discrepancy between the industrial bending test usually considered and the walking or running application.

Acknowledgement

The work is part of the PhD of A.J. supported by the Chair "Modeling advanced polymers for innovative material solutions" led by Ecole polytechnique (l'X) and the Fondation de l'Ecole polytechnique and sponsored by Arkema. The authors would like to gratefully acknowledge Pierre Jolivet for his advice and assistance with parallel computing using PETSc and FreeFem++.

Replication of results

The authors agree to share the 3D sole CAD model [62]. The code described in this paper is written with an open source software, additional details can be made available upon request.

Appendix A Expression of the bilinear forms

The displacement u represents the vertical displacement in 2D and $u = (u_1, u_2, u_3)$ in 3D. For $n \in \mathbb{N}_+^*$ and $(\omega, u) \in \mathbb{C} \times \mathcal{U}_0$, the complex polynomial eigenproblem reads:

$$\sum_{j=0}^{n+2} \omega^j a_j(u, \hat{u}) = 0 \qquad \forall \hat{u} \in \mathcal{U}_0.$$

We denote for the Kirchhoff-Love theory

$$\varphi(u, \hat{u}) = \frac{\partial^2 u}{\partial x_1^2}\frac{\partial^2 \hat{u}}{\partial x_1^2} + \frac{\partial^2 u}{\partial x_2^2}\frac{\partial^2 \hat{u}}{\partial x_2^2}$$

$$\psi(u, \hat{u}) = \frac{\partial^2 u}{\partial x_1^2}\frac{\partial^2 \hat{u}}{\partial x_2^2} + \frac{\partial^2 u}{\partial x_2^2}\frac{\partial^2 \hat{u}}{\partial x_1^2}$$

$$\xi(u, \hat{u}) = \frac{\partial^2 u}{\partial x_1 \partial x_2}\frac{\partial^2 \hat{u}}{\partial x_1 \partial x_2},$$

for the Reissner-Mindlin theory

$$\varphi(u, \hat{u}) = \frac{\partial \theta_1}{\partial x_1}\frac{\partial \hat{\theta}_x}{\partial x_1} + \frac{\partial \theta_2}{\partial x_2}\frac{\partial \hat{\theta}_y}{\partial x_2}$$

$$\psi(u, \hat{u}) = \frac{\partial \theta_1}{\partial x_1}\frac{\partial \hat{\theta}_y}{\partial x_2} + \frac{\partial \theta_2}{\partial x_2}\frac{\partial \hat{\theta}_x}{\partial x_1}$$

$$\xi(u, \hat{u}) = \left(\frac{\partial \theta_1}{\partial x_2} + \frac{\partial \theta_2}{\partial x_1}\right)\left(\frac{\partial \hat{\theta}_x}{\partial x_2} + \frac{\partial \hat{\theta}_y}{\partial x_1}\right),$$

and for the 3D linear viscoelastic model

$$\varphi(u, \hat{u}) = \frac{\partial u_1}{\partial x_1}\frac{\partial \hat{u}_1}{\partial x_1} + \frac{\partial u_2}{\partial x_2}\frac{\partial \hat{u}_2}{\partial x_2} + \frac{\partial u_3}{\partial x_3}\frac{\partial \hat{u}_3}{\partial x_3}$$

$$\psi(u, \hat{u}) = \left(\frac{\partial u_2}{\partial x_2} + \frac{\partial u_3}{\partial x_3}\right)\frac{\partial \hat{u}_1}{\partial x_1} + \left(\frac{\partial u_1}{\partial x_1} + \frac{\partial u_3}{\partial x_3}\right)\frac{\partial \hat{u}_2}{\partial x_2} + \left(\frac{\partial u_1}{\partial x_1} + \frac{\partial u_2}{\partial x_2}\right)\frac{\partial \hat{u}_3}{\partial x_3}$$

$$\begin{aligned}\xi(u, \hat{u}) = &\left(\frac{\partial u_1}{\partial x_2} + \frac{\partial u_2}{\partial x_1}\right)\left(\frac{\partial \hat{u}_1}{\partial x_2} + \frac{\partial \hat{u}_2}{\partial x_1}\right) + \left(\frac{\partial u_1}{\partial x_3} + \frac{\partial u_3}{\partial x_1}\right)\left(\frac{\partial \hat{u}_1}{\partial x_3} + \frac{\partial \hat{u}_3}{\partial x_1}\right) \\ &+ \left(\frac{\partial u_2}{\partial x_3} + \frac{\partial u_3}{\partial x_2}\right)\left(\frac{\partial \hat{u}_2}{\partial x_3} + \frac{\partial \hat{u}_3}{\partial x_2}\right).\end{aligned}$$

Symmetric bilinear forms are given by

$$a_0(u,\hat{u}) = \int_\Omega -\frac{h^3}{12}\frac{E_0}{(1-\nu_0^2)}\left(\varphi(u,\hat{u}) + \nu_0\psi(u,\hat{u}) + 2(1-\nu_0)\xi(u,\hat{u})\right)dx$$

$$\begin{aligned} a_1(u,\hat{u}) = &\int_\Omega -\frac{h^3}{12}p_1\sum_{k=0}^{n}\frac{E_k}{1-\nu_k^2}\left(\varphi(u,\hat{u}) + \nu_k\psi(u,\hat{u}) + 2(1-\nu_k)\xi(u,\hat{u})\right)dx \\ &+ \int_\Omega \frac{h^3}{12}\sum_{k=1}^{n} q_{1,k}\frac{E_k}{1-\nu_k^2}\left(\varphi(u,\hat{u}) + \nu_k\psi(u,\hat{u}) + 2(1-\nu_k)\xi(u,\hat{u})\right)dx \end{aligned}$$

$\forall j \in [\![2, n-1]\!]$,

$$\begin{aligned} a_j(u,\hat{u}) = &\int_\Omega p_{j-2}\rho h u\hat{u}\,dx \\ &- \int_\Omega \frac{h^3}{12}p_j\sum_{k=0}^{n}\frac{E_k}{1-\nu_k^2}\left(\varphi(u,\hat{u}) + \nu_k\psi(u,\hat{u}) + 2(1-\nu_k)\xi(u,\hat{u})\right)dx \\ &+ \int_\Omega \frac{h^3}{12}\sum_{k=1}^{n} q_{j,k}\frac{E_k}{1-\nu_k^2}\left(\varphi(u,\hat{u}) + \nu_k\psi(u,\hat{u}) + 2(1-\nu_k)\xi(u,\hat{u})\right)dx \end{aligned}$$

$$\begin{aligned} a_n(u,\hat{u}) = &\int_\Omega p_{n-2}\rho h u\hat{u}\,dx \\ &- \int_\Omega \frac{h^3}{12}p_n\sum_{k=0}^{n}\frac{E_k}{1-\nu_k^2}\left(\varphi(u,\hat{u}) + \nu_k\psi(u,\hat{u}) + 2(1-\nu_k)\xi(u,\hat{u})\right)dx \end{aligned}$$

$$a_{n+1}(u,\hat{u}) = \int_\Omega p_{n-1}\rho h u\hat{u}\,dx$$

$$a_{n+2}(u,\hat{u}) = \int_\Omega p_n\rho h u\hat{u}\,dx.$$

In the above, the coefficients p_j and $q_{j,k}$ are defined through the expansions

$$\prod_{j=1}^{n}(1+i\omega\tau_j) = \sum_{j=0}^{n} p_j\omega^j$$

$$\prod_{\substack{j=1\\ j\neq k}}^{n}(1+i\omega\tau_j) = \sum_{j=0}^{n} q_{j,k}\omega^j.$$

Conflict of interest

On behalf of all authors, the corresponding author states that there is no conflict of interest.

References

[1] Ward, I.M., Sweeney, J.: An Introduction to the Mechanical Properties of Solid Polymers, 2nd edn., p. 394. Wiley, Hoboken, New Jersey (2004)

[2] Shimoyama, K., Seo, K., Nishiwaki, T., Jeong, S., Obayashi, S.: Design optimization of a sport shoe sole structure by evolutionary computation and finite element method analysis. Proceedings of the Institution of Mechanical Engineers, Part P: Journal of Sports Engineering and Technology **225**, 179–188 (2011). https://doi.org/10.1177/1754337111414485

[3] Nishiwaki, T.: Running shoe sole stiffness evaluation method based on eigen vibration analysis. Sports Technology **1**(1), 76–82 (2008). https://doi.org/10.1080/19346182.2008.9648453

[4] Allaire, G.: Conception Optimale de Structures. Mathématiques et Applications, vol. 58, p. 280. Springer, Berlin Heidelberg (2007)

[5] Allaire, G., Dapogny, C., Jouve, F.: Shape and topology optimization. Handbook of Numerical Analysis. Geometric partial differential equations, part II. A. Bonito and R.H. Nochetto eds., pp. 1–132. Elsevier, Amsterdam, The Netherlands (2021)

[6] Bendsøe, M., Sigmund, O.: Topology Optimization: Theory, Methods, and Applications. Springer, New York (2013)

[7] Allaire, G., Jouve, F.: A level-set method for vibration and multiple loads structural optimization. Computer Methods in Applied Mechanics and Engineering **194**, 3269–3290 (2005). https://doi.org/10.1016/j.cma.2004.12.018

[8] Ma, Z.D., Kikuchi, N., Hagiwara, I.: Structural topology and shape optimization for a frequency response problem. Computational mechanics **13**(3), 157–174 (1993). https://doi.org/10.1007/BF00370133

[9] Ogawa, S., Yamada, T.: Topology optimization for transient response problems involving thermoelastic materials. Finite Elements in Analysis and Design **201** (2022). https://doi.org/10.1016/j.finel.2021.103695

[10] Andreassen, E., Jensen, J.S.: Topology optimization of periodic microstructures for enhanced dynamic properties of viscoelastic composite materials. Structural and Multidisciplinary Optimization **49**, 695–705

(2013). https://doi.org/10.1007/s00158-013-1018-2

[11] Elsabbagh, A., Baz, A.: Topology optimization of unconstrained damping treatments for plates. Engineering Optimization **46**, 1153–1168 (2014). https://doi.org/10.1080/0305215X.2013.832235

[12] Kang, Z., Zhang, X., Jiang, S., Cheng, G.D.: On topology optimization of damping layer in shell structures under harmonic excitations. Structural and Multidisciplinary Optimization **46**, 51–67 (2011). https://doi.org/10.1007/s00158-011-0746-4

[13] Chen, W., Liu, S.: Microstructural topology optimization of viscoelastic materials for maximum modal loss factor of macrostructures. Structural and Multidisciplinary Optimization **53**, 1–14 (2015). https://doi.org/10.1007/s00158-015-1305-1

[14] Fang, Z., Yao, L., Tian, S., Hou, J.: Microstructural topology optimization of constrained layer damping on plates for maximum modal loss factor of macrostructures. Shock and Vibration **2**, 1–13 (2020). https://doi.org/10.1155/2020/8837610

[15] Liu, Q., Ruan, D., Huang, X.: Topology optimization of viscoelastic materials on damping and frequency of macrostructures. Computer Methods in Applied Mechanics and Engineering **337**, 305–323 (2018). https://doi.org/10.1016/j.cma.2018.03.044

[16] Fang, Z., Zheng, L.: Topology optimization for minimizing the resonant response of plates with constrained layer damping treatment. Shock and Vibration **2015**, 11 (2015). https://doi.org/10.1155/2015/376854

[17] Ansari, M., Khajepour, A., Esmailzadeh, E.: Application of level set method to optimal vibration control of plate structures. Journal of Sound and Vibration **332**(4), 687–700 (2013). https://doi.org/10.1016/j.jsv.2012.09.006

[18] Delgado, G., Hamdaoui, M.: Topology optimization of frequency dependent viscoelastic structures via a level-set method. Applied Mathematics and Computation **347**, 522–541 (2019). https://doi.org/10.1016/j.amc.2018.11.014

[19] Joubert, A., Allaire, G., Amstutz, S., Diani, J.: Damping optimization of viscoelastic cantilever beams and plates under free vibration. Computers & Structures **268**(3) (2022). https://doi.org/10.1016/j.compstruc.2022.106811

[20] Belblidia, F., Lee, J.E.B., Rechak, S., Hinton, E.: Topology optimization of plate structures using a single- or three-layered artificial material model.

Advances in Engineering Software **32**, 159–168 (2001). https://doi.org/10.1016/S0045-7949(00)00141-3

[21] Horio, H., Kogiso, N., Otomori, M., Yamada, T., Nishiwaki, S.: Level set-based topology optimization of thin plate structure for maximizing stiffness under out-of-plane deformation. Transactions of the JSME **80**(811) (2014). https://doi.org/10.1299/transjsme.2014dsm0054

[22] Khoza, D.: Topology optimization of plate-like structures. University of Pretoria (2006)

[23] Li, S.L., Long, S.Y., Li, G.Y.: A Topology Optimization of Moderately Thick Plates Based on the Meshless Numerical Method. Computer Modeling in Engineering and Sciences **60**(1), 73–94 (2010). https://doi.org/10.3970/cmes.2010.060.073

[24] Arnold, D.N., Madureira, A.L., Zhang, S.: On the Range of Applicability of the Reissner-Mindlin and Kirchhoff-Love Plate Bending Models. Journal of Elasticity **67**, 171–185 (2002). https://doi.org/10.1023/A:1024986427134

[25] Hughes, T.J.R.: The Finite Element Method: Linear Static and Dynamic Finite ElementAnalysis, p. 704. Prentice-Hall, Inc., Englewood Cliffs, NJ (1987)

[26] Carvalho, F.S., Ruscheinsky, D., Giusti, S.M., Anflor, C.T.M., Novotny, A.A.: Topological derivative-based topology optimization of plate structures under bending effects. Structural and Multidisciplinary Optimization **63** (2021). https://doi.org/10.1007/s00158-020-02710-4

[27] Dal Poggetto, V.F., Arruda, J.R.F.: Widening wave band gaps of periodic plates via shape optimization using spatial fourier coefficients. Mechanical Systems and Signal Processing **147** (2021). https://doi.org/10.1016/j.ymssp.2020.107098

[28] Timoshenko, S., Wolnowsky-Krieger, S.: Theory of Plates and Shells, 2nd edn., p. 580. McGraw-Hill College, New York (1959)

[29] Haug, E., Rousselet, B.: Design Sensitivity Analysis in Structural Mechanics.II. Eigenvalue Variations. Journal of Structural Mechanics **8**(2), 161–186 (1980). https://doi.org/10.1080/03601218008907358

[30] Olhoff, N., Seyranian, A.P., Lund, E.: Multiple eigenvalues in structural optimization problems. Structural optimization **8**, 207–227 (1980). https://doi.org/10.1007/BF01742705

[31] Gröhlich, M., Lang, A., Böswald, M., Meier, J.: Viscoelastic damping

design - thermal impact on a constrained layer damping treatment. Materials and Design **207**, 109885 (2021). https://doi.org/10.1016/j.matdes.2021.109885

[32] Rowbottom, M.D.: The optimization of mechanical dampers to control self-excited galloping oscillations. Journal of Sound and Vibration **75**, 559–576 (1981). https://doi.org/10.1016/0022-460X(81)90442-9

[33] Ammari, K., Henrot, A., Tucsnak, M.: Asymptotic behaviour of the solutions and optimal location of the actuator for the pointwise stabilization of a string. Asymptotic Analysis **28**, 215–240 (2001)

[34] Freitas, P.: Optimizing the rate of decay of solutions of the wave equation using genetic algorithms: A counterexample to the constant damping conjecture. SIAM Journal on Control and Optimization **37**, 376–387 (1999). https://doi.org/10.1137/S0363012997329445

[35] Simon, J., Murat, F.: Etudes de problèmes d'optimal design, vol. 41, pp. 54–62. Springer, Berlin (1976)

[36] Henrot, A., Pierre, M.: Shape Variation and Optimization : a Geometrical Analysis. Tracts in Mathematics, vol. 28, p. 379. European Mathematical Society, Helsinki, Finland (2018). https://doi.org/10.4171/178

[37] Hecht, F.: New development in freefem++. Journal of Numerical Mathematics **20**, 251–266 (2012). https://doi.org/10.1515/jnum-2012-0013

[38] Morley, L.S.D.: A triangular equilibrium element with linearly varying bending moments for plate bending problems. Journal of the Royal Aeronautical Society **71**, 715–719 (1967). https://doi.org/10.1017/S0001924000054373

[39] Morley, L.S.D.: The triangular equilibrium element in the solution of plate bending problems. Aeronautical Quarterly **19**, 149–169 (1968). https://doi.org/10.1017/S0001925900004546

[40] Hernández, V., Román, J., Vidal, V.: SLEPc: A scalable and flexible toolkit for the solution of eigenvalue problems. ACM Transactions on Mathematical Software **31**, 351–362 (2005). https://doi.org/10.1145/1089014.1089019

[41] Dolean, V., Jolivet, P., Nataf, F.: An Introduction to Domain Decomposition Methods. Algorithms, Theory, and Parallel Implementation. Philadelphia, PA: Society for Industrial and Applied Mathematics (SIAM), vol. 144 (2015)

[42] Jolivet, P., Dolean, V., Hecht, F., Nataf, F., Prud'Homme, C., Spillane, N.:

High performance domain decomposition methods on massively parallel architectures with freefem++. Journal of Numerical Mathematics **20**(3-4), 287–302 (2012). https://doi.org/10.1515/jnum-2012-0015

[43] Osher, S.J., Sethian, J.A.: Fronts propagating with curvature-dependent speed: algorithms based on hamilton-jacobi formulations. Journal of Computational Physics **79**(1), 12–49 (1988). https://doi.org/10.1016/0021-9991(88)90002-2

[44] Allaire, G., Jouve, F., Toader, A.M.: A level-set method for shape optimization. Comptes Rendus Mathematiques **334**(12), 1125–1130 (2002). https://doi.org/10.1016/S1631-073X(02)02412-3

[45] Osher, S.J., Santosa, F.: Level-set methods for optimization problems involving geometry and constraints. Journal of Computational Physics **171**(1), 272–288 (2001). https://doi.org/10.1006/jcph.2001.6789

[46] Bui, C., Dapogny, C., Frey, P.: Advect. GitHub (2015)

[47] Nocedal, J., Wright, S.J.: Numerical Optimization, 2nd edn., p. 664. Springer, New York (2006)

[48] Villanueva, C.H., Maute, K.: Density and level set-XFEM schemes for topology optimization of 3-D structures. Computational Mechanics **54**(1), 133–150 (2014). https://doi.org/10.1007/s00466-014-1027-z

[49] Burman, E., Claus, S., Hansbo, P., Larson, M.G., Massing, A.: CutFEM: discretizing geometry and partial differential equations. International Journal for Numerical Methods in Engineering **104**(7), 472–501 (2015). https://doi.org/10.1002/nme.4823

[50] Dapogny, C., Dobrzynski, C., Frey, P.: Three-dimensional aptive domain remeshing, implicit domain meshing, and applications to free and moving boundary problems. Journal of Computational Physics **262**, 358–378 (2014). https://doi.org/10.1016/j.jcp.2014.01.005

[51] Weller, H., Jasak, H.: OpenFOAM Web page. https://www.openfoam.com/documentation/guides/latest/doc/guide-solvers-multigrid-gamg.html (2004)

[52] Saad, Y., Schultz, M.H.: Gmres: A generalized minimal residual algorithm for solving nonsymmetric linear systems. SIAM Journal on Scientific and Statistical Computing **7**(3), 856–869 (1986). https://doi.org/10.1137/0907058

[53] Amestoy, P.R., Buttari, A., L'Excellent, J.Y., Mary, T.: Performance and Scalability of the Block Low-Rank Multifrontal Factorization on Multicore

Architectures. ACM Transactions on Mathematical Software **45**(1), 2–1226 (2019). https://doi.org/10.1145/3242094

[54] Amestoy, P.R., Duff, I.S., Koster, J., L'Excellent, J.Y.: A fully asynchronous multifrontal solver using distributed dynamic scheduling. SIAM Journal on Matrix Analysis and Applications **23**(1), 15–41 (2001). https://doi.org/10.1137/S0895479899358194

[55] Chevalier, C., Pellegrini, F.: PT-Scotch: A tool for efficient parallel graph ordering. Parallel Computing **34**(6-8), 318–331 (2008). https://doi.org/10.1016/j.parco.2007.12.001

[56] Pellegrini, F.: Scotch and PT-Scotch Graph Partitioning Software: An Overview. In: Uwe Naumann, O.S. (ed.) Combinatorial Scientific Computing, pp. 373–406. Chapman and Hall/CRC, London (2012). https://doi.org/10.1201/b11644-15

[57] Karypis, G., Kumar, V.: METIS A Software Package for Partitioning Unstructured Graphs, Partitioning Meshes, and Computing Fill-Reducing Orderings of Sparse Matrices. Computer Science & Engineering, Technical Report 97-061, p. 31 (1997)

[58] Allaire, G., Jouve, F., Michailidis, G.: Thickness control in structural optimization via a level set method. Structural and Multidisciplinary Optimization **53**(6), 1349–1382 (2016). https://doi.org/10.1007/s00158-016-1453-y

[59] Dapogny, C., Faure, A., Michailidis, G., Allaire, G., Couvelas, A., Estevez, R.: Geometric constraints for shape and topology optimization in architectural design. Computational Mechanics **59**, 933–965 (2017). https://doi.org/10.1007/s00466-017-1383-6

[60] Geuzaine, C., Remacle, J.F.: Gmsh: a three-dimensional finite element mesh generator with built-in pre- and post-processing facilities. International Journal for Numerical Methods in Engineering **79**(11), 1309–1331 (2009)

[61] Dassault Systèmes: CATIA Web page. https://www.3ds.com/products-services/catia/ (1981)

[62] Joubert, A., Allaire, G., Amstutz, S., Diani, J.: Shoe sole CAD model. CAD file (2023). https://hal.science/hal-04018469